Nonlinear Analysis of Soil Response Under Dynamic Shear Loading

A Comparison with Experimental Resonant Column Test Data

Riccardo Mei

5615763

Thesis Committee:

Ass. Prof. Karel van Dalen	TU Delft
Dr. Andrei Fărăgău	TU Delft
Dr. Evangelos Kementzetzidis	TU Delft
Ir. Lukas Huber	TU Delft
Ir. Stavros Panagoulias	TU Delft, Siemens Gamesa

14th February 2025

Delft University of Technology

Civil Structural Engineering

Hydraulic Structures Track

Acknowledgements

Firstly, I want to thank all my committee members. Each of you has been crucial to the positive outcome of my thesis with your immense knowledge of the topic and your constant advice. In moments of doubt, when someone reconsiders his life choices, you have been the motivation to keep going despite the difficulties. The thought of changing plans and, potentially, having to change the committee was simply not an option. You have done more than was expected from you for me and I appreciate this greatly.

To all the friends of “Alcoholics” met on the first day of TU Delft. The ones that have started this journey with me and are still here for me.

To the Caravelle, the Bachelor friends made in Parma. The ones that have started this journey with me and have now travelled all the way. Thanks for all the trips you made to come over to visit, and especially for being here in person today. Those real friends that last in the years and those friendships that never change.

To the Poveri. What started as a football team but became to all effects a fraternity. Fraternity because you have been my brothers here in Delft. In these years, we went from teammates to friends for nights out, to companions for trips across Europe and have become a housing agency, which in Delft is always handy to have. TU Delft has never seen a group of “students” dominating every game like we do and I wish it could go on forever.

To the friends of Delft Core. Despite all of us choosing our paths, we still refuse to leave university life. Thank you for the daily contact, that could be a simple beer, to break the monotony of daily life. And, especially, for motivating me to run the half-marathon together.

To Enrico, Ziug. Thank you for the incredible time spent together before you became a travel blogger, working in every country of the world. From the pasta cooked directly in the boiler to the evening saunas where we could gossip forever.

To Matilde, for the support and the texts in the difficult times. The friendship started as kid when we were living in Dublin and is till the same today.

To my housemates, the inhabitants of the jungle as we are known, for making the house feel like home. For the dinners together, the chats late at night where a simple knock on the door was sufficient to start a never-ending conversation.

And my almost-housemates, who officially didn’t pay the rent but were still always there. Stefano, the lion, for the songs played with guitars in the living room. Alessio, my Gemellino, for the original gardening sessions, entertaining the old neighbours.

To Abi, the friend that you casually met by mistake because we were the only two idiots going to a cancelled lecture. And Celia, the friend that you meet because none of you ever stops talking. The type of people that have the most genuine heart. The ones that you blindly count on in every moment of your day but also in my future life.

To all my family.

My uncle, aunt and 2 little cousins. Sorry for not spending together all the time I wished for during Christmas. The many “no” I had to say to hand in the thesis in time. A special recognition to the youngest of the family, Fede, for offering to lend me his coloured pencils to colour my thesis.

My two brothers, for sending memes on Instagram mocking engineers, reminding me how normal people view us.

Parents, for supporting me in times of indecision and patiently waiting for me to find my path.

Finally, I would like to thank all my grandparents, to whom this thesis is dedicated to. To the ones who couldn’t be there physically but managed to connect online at the age of 88. To my granddad who passed away during my master's but has transmitted me the passion for this job. And finally, you Nonna, that have always been there for me in every important moment of my life. I’m sorry if I had promised you to become a vet in life so that we could go care for the elephants together. I guess you have to forgive me for becoming an engineer in the end.

Abstract

Understanding the dynamic behaviour of soil is crucial for the design of geotechnical structures, particularly for offshore wind turbine foundations. This study evaluates the performance of a nonlinear numerical model in accurately capturing soil response under dynamic shear loading, comparing its simulated response to experimental data obtained from Resonant Column Tests (RCT). The research systematically investigates the role of higher-order odd harmonics in the numerical solution, assesses the differences between linear and nonlinear models, and validates the nonlinear model against experimental results.

The findings reveal that higher-order harmonics contribute negligibly to the numerical response, simplifying the model's implementation. Furthermore, the nonlinear model effectively captures the resonance shift observed in experimental data, outperforming the linear model, particularly at higher strain levels where soil softening effects become significant. While the model demonstrates a strong correlation with experimental results, discrepancies arise in high-strain scenarios, primarily due to limitations in damping representation. To address this, corrective approaches such as a damping correction factor and strain radius adjustments were explored, improving model accuracy but failing to eliminate errors entirely. The study highlights the necessity of incorporating a strain-dependent damping formulation to enhance predictive capabilities for high-strain soil behaviour.

The results confirm that nonlinear numerical modelling is a valuable tool for capturing essential soil dynamics, but further refinements in damping representation are required to improve alignment with experimental data. Future research should focus on advanced damping models to ensure greater accuracy in high-strain dynamic soil simulations.

Contents

List of Figures

List of Variables

Symbol	Variables	Units
x	Axial coordinate	$[m]$
r	Radial distance from the centre of the specimen	$[m]$
θ	Angle of rotation of horizontal cross-sections	$[rad]$
r_{obs}	Observation radius	$[m]$
Δ	Linear displacement	$[m]$
γ	Linear strain	$[-]$
ρ	Soil density	$[kg/m^3]$
G	Shear elastic modulus	$[MPa]$
G_0	Initial shear elastic modulus	$[MPa]$
η	Damping coefficient	$[kg/m/s]$
ζ	Damping ratio	$[-]$
Ω	Frequency of excitation	$[rad/s]$
$\mathrm{T_s}$	Torque along the specimen	$[Nm]$
Ip	Polar area moment of inertia	$[kg\,m^4]$
Js	Specimen polar mass moment of inertia	$[kg\,m^2]$
I_{active}	Active plate's inertia	$[kg\,m^4]$
Ja	Active plate's polar mass moment of inertia	$[kg\,m^2]$
T_0	Torque amplitude	$[Nm]$
T_M	Motor's torque excitation	$[Nm]$
γ_{ref}	Reference linear strain	$[-]$
β	Decay constant	$[-]$
T	Period	$[s]$
p'	Mean effective stress	$[kPa]$

Superscripts	
$\ddot{x}$	Time derivative
$\dot{x}$	Double time derivative
x'	Spatial derivative
x''	Double spatial derivative
$\bar{x}$	Vector
$\bar{\bar{x}}$	Matrix

Abbreviations	
HBM	Harmonic Balance Method
RCT	Resonant Column Test
DCF	Damping Correction Factor

Chapter 1 – Introduction

1.1 Background

With the rapid rise in global energy consumption, production is struggling to meet the demand. Therefore, major plans are being made worldwide in order to increase electrical power production for the future years. Simultaneously, global warming has sparked interest in sustainable and clean energy. The EU has formulated its policies such as The European Green Deal, to tackle this problem and reach net zero emissions by 2050 [1].

Due to this push for renewable energy, wind energy has seen exponential growth in recent years and is expected to follow this trend in the coming years. Despite both the onshore and offshore wind energy sectors experiencing considerable investment and development, offshore wind projects are of greater significance due to their better efficiency than onshore installations. A study by the International Energy Agency showed that alone the best close-to-shore offshore wind sites globally could provide the global electricity demand projected for 2040. The shallow coastal water together with the favourable wind conditions and the limited land availability are all factors that make the North Sea an ideal location for the wind farm construction.

Offshore wind turbines are installed through various foundation types, each differing in cost, depth, and functionality. Monopiles, gravity-base, jackets, semi-submersible and floating are the most common types of foundations found worldwide. Among these, monopile foundations are the most cost-effective and straightforward to install, though they are depth-limited. Where feasible, monopiles are therefore the preferred foundation choice. As for 2019, monopiles accounted for 81% of offshore wind turbine foundations and were also the most popular substructure type among all newly installed foundations [2].

The monopile is a hollow cylindrical structure, that driven into the underlying seabed, supports the wind turbine tower above. The monopile must withstand all forces generated by wind and waves transferred through the structure to the underlying seabed. Beyond ensuring this structural requirement, it is critical to maintain the structure's natural frequency distinct from the excitation frequencies of these external forces. If the natural frequency of the wind turbine aligns with that of external forces, resonance may occur, potentially leading to structural failure.

The external forcing frequencies may resonate with two different frequencies characteristic of the wind turbine structure:

- 1P: The primary excitation frequency of the wind turbine triggered by the rotational speed of the rotor.

- 3P: The second excitation frequency is caused when the single blade passes by the vertical tower, causing additional cyclic load on the structure.

The 1P and 3P frequencies together with the wave and wind spectra may be visualised in Figure 1.

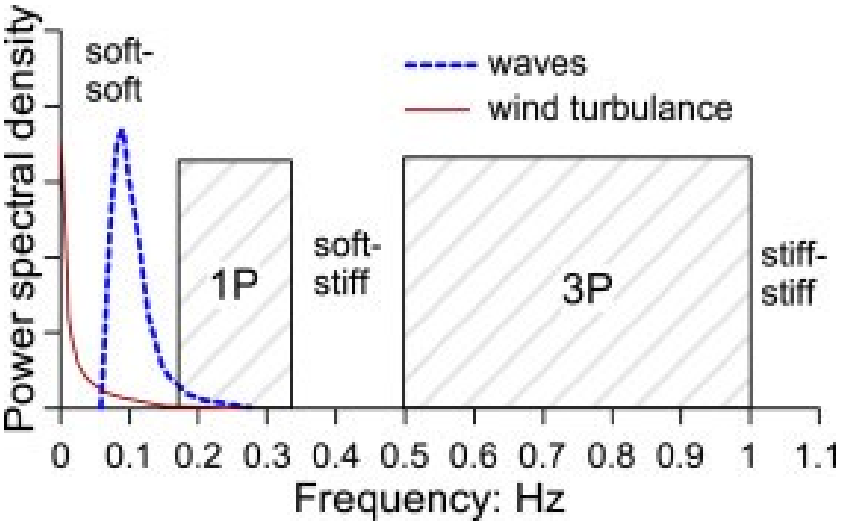

Figure 1 – Excitation frequencies acting on a typical wind turbine system *[3]*

The soil's properties significantly influence the structure's natural frequency. Therefore, in designing offshore wind turbines, thoroughly understanding soil behaviour is key to limiting the interference of natural frequencies with excitation frequencies and avoiding over-dimensioning.

1.2 Problem Statement and Objectives

Accurate soil modelling is crucial during the design phase of a monopile foundation. The behaviour of the soil can be studied with laboratory experiments, such as Resonance Column Tests, where it is possible to replicate the seabed loading conditions. However, these tests are often expensive and time-consuming.

Consequently, simulating real-life behaviour through modelling is a more practical approach. Existing models, even if computationally efficient, often rely on simplifications that compromise the accuracy of the results. This thesis aims to develop a numerical model capable of accurately simulating nonlinear soil behaviour under dynamic forcing conditions and comparing it with experimental data obtained in Resonance Column Tests, without increasing the computational time excessively.

1.3 Objectives

The objective of this study is to evaluate the performance of a nonlinear numerical model in accurately capturing soil behaviour under dynamic loading conditions. The goal is to compare the model’s simulated response with experimental data provided by the RCT. Specifically, this research aims to:

1. **Assess the Contribution of Super-Harmonics**: Investigate the influence of higher-order odd harmonics (third and fifth) on the numerical solution and determine their relevance in different strain states to simplify model implementation.
2. **Compare Linear and Nonlinear Models**: Analyse the significance of incorporating nonlinear material behaviour in numerical simulations and its effect on capturing resonance shifts observed in experimental data.
3. **Validate the Nonlinear Model Against Experimental Data**: Examine the accuracy of the nonlinear model in reproducing soil response across different strain levels, identifying strengths and limitations, particularly in high-strain scenarios.
4. **Evaluate Discrepancies and Model Limitations**: Identify and analyse model inaccuracies, particularly in damping representation, and explore potential corrective measures. The adjustments proposed should either improve the results of the model or give a better understanding of the corrections to be made.

1.4 Research Questions

Therefore, the research questions to be answered in this thesis are:

- How do super-harmonics harmonics influence the numerical solution of soil response under dynamic loading, and to what extent can they be disregarded in different strain states without compromising model accuracy?
- How does the incorporation of nonlinear material behaviour affect the accuracy of numerical simulations in capturing resonance shifts, and how does it compare to a linear model in terms of computational efficiency?
- To what extent does the nonlinear numerical model accurately reproduce experimental soil response across varying strain levels, and what are the key strengths and limitations in its predictive capability, particularly at high-strain states?

1.5 Research outline

This section provides an overview of the subsequent chapters of this thesis, outlining their content and purpose.

Chapter 2 presents a comprehensive review of the existing literature and previous research relevant to this study. The key theoretical concepts underlying the research are discussed to establish the necessary foundation before addressing the problem at hand.

Chapter 3 details the formulation of the models, providing a rigorous exposition of their mathematical structure. This chapter systematically develops the theoretical framework of both the linear and nonlinear models, necessary for the subsequent analysis.

Chapter 4 describes the experimental data employed to validate the simulated results of the model. Specifically, it outlines the nature and sources of the data, as well as the methodology used for data acquisition. Additionally, this chapter discusses the preprocessing steps required to ensure compatibility between the experimental data and the simulated results for meaningful comparison.

Chapter 5 presents and analyses the results of the study. The discussion begins with an examination of the super-harmonic contributions to the total signal. Subsequently, a comparative analysis between linear and nonlinear models is conducted, followed by an evaluation of the experimental data concerning the nonlinear model. Finally, a parametric modification of the model is explored to assess its impact on improving the accuracy of the results.

Chapter 6 provides the conclusions of the thesis, summarizing the key findings and their implications.

Chapter 7 offers recommendations for potential future developments and extensions of this research.

Chapter 2 – Literature Study

2.1 Constitutive Soil Models

In the attempt to describe the stress-strain relationship in soil, several constitutive models can be considered, each able to capture different behaviours of the soil. The three main constitutive models, represented in Figure 2, used to represent soil behaviour can generally be classified into three categories: linear, nonlinear, and hysteretic models. These models attempt to describe how soil deforms and resists external forces, considering different factors such as elasticity, plasticity, strain rate, and cyclic loading effects. There is no "better" model to use, as selecting an appropriate constitutive soil model depends on the nature of the problem, loading conditions, and soil type.

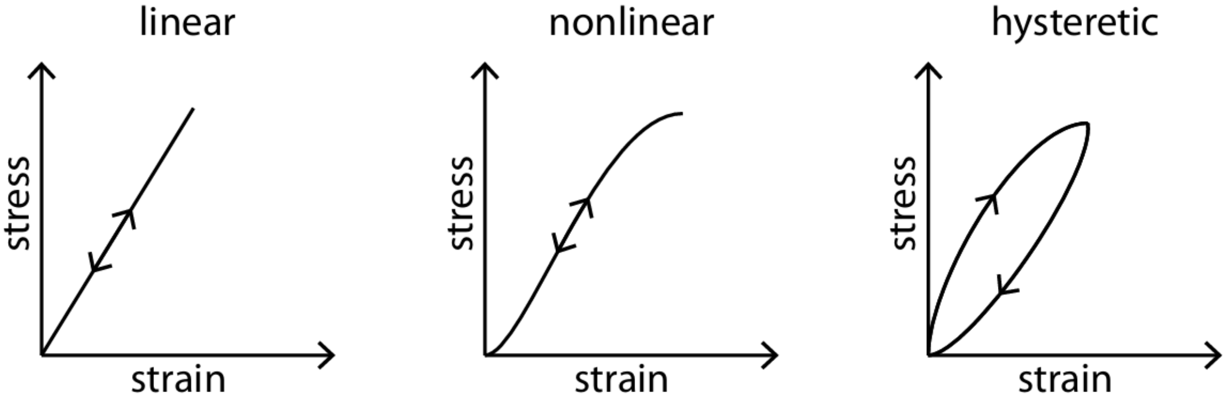

Figure 2 – Stress-strain relationships in soil modelling *[4]*

2.1.1 Linear Soil Models

Linear soil models assume a proportional relationship between stress and strain, following Hooke's Law. This simplification is typically applied to elastic materials, where deformations are small and fully recoverable upon unloading. The model presented by Wood [5] characterizes soil using two material parameters, Young's modulus (E) and Poisson's ratio (ν). It is widely used in first-order approximations for stress analysis in soils with small strains.

While linear models are useful for preliminary analysis, they fail to capture the inelastic behaviour of soils, crucial when analysing high-strain states.

2.1.2 Nonlinear Soil Models

Nonlinear models are necessary to describe the stress-strain relationship of soil beyond the elastic limit, where deformation is not proportional to applied stress. These models incorporate plasticity, stress history, and strain-dependent stiffness. The model described by Vardoulakis [6], accounts for progressive failure mechanisms in soils, particularly relevant for landslide analysis and post-peak behaviour. Another empirical model describes the nonlinear relationship between stress and strain using a hyperbolic function, effectively representing soil stiffness degradation under increasing load [7].

2.1.3 Hysteretic Soil Models

Hysteretic models are particularly important for describing soil behaviour under cyclic or dynamic loading, such as earthquakes, machine vibrations, and wave-soil interactions. Unlike linear or nonlinear models, hysteretic models explicitly capture energy dissipation and path-dependent behaviour. Hysteretic models are crucial for earthquake engineering and dynamic soil-structure interaction problems, where cyclic degradation and energy dissipation play significant roles.

2.2 Damping Models

Damping is a critical aspect of soil modelling as it influences the dynamic response of soil-structure systems under external loading conditions. Various damping models have been proposed to characterize energy dissipation in soil, primarily categorized into viscous damping, hysteretic damping, and radiation damping. Furthermore, hybrid models are being tested, where combinations of these models are combined. Each of these models has distinct theoretical foundations and applications in geotechnical engineering.

2.2.1 Viscous Damping

Viscous damping represents energy dissipation as a function of velocity-dependent forces, commonly applied in linear dynamic analyses. The Rayleigh Damping Model approach, used in finite element analysis (FEA), is defined as a linear combination of mass-proportional and stiffness-proportional damping. However, it has been criticized for its frequency-dependent nature, leading to potential inaccuracies when applied to multi-modal dynamic analyses.

2.2.2 Hysteretic Damping

Hysteretic damping models account for the energy dissipation due to inelastic deformation of soil particles. These models are widely used in seismic soil-structure interaction (SSI) studies and pile foundation dynamics. Many hysteretic damping models rely on the Masing rule, illustrated in Figure 3, which assumes that stress-strain curves during cyclic loading follow the same loading-unloading paths as the primary stress-strain relationship. Shirzoi et al. [8] have refined these models to better simulate nonlinear soil behaviour under cyclic loading. The Modified Davidenkov Model, described by Zhou et al. [9], introduces strain-dependent damping ratios, improving its accuracy in predicting soil behaviour under large-strain conditions.

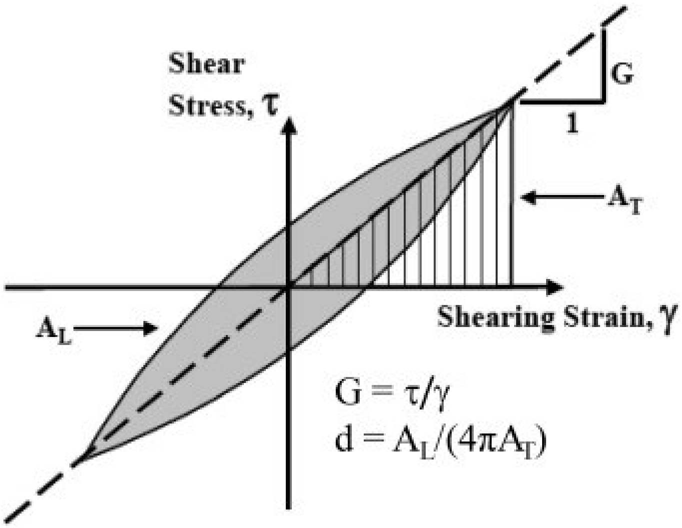

Figure 3 – Definition of hysteretic damping at the soil element level *[10]*

2.2.3 Radiation Damping Models

Radiation damping accounts for energy loss due to the outward propagation of stress waves from a vibrating structure into the surrounding soil. This phenomenon is crucial in foundation dynamics and offshore geotechnical engineering. Wang et al. [11] proposed a soil models that incorporate frequency-dependent radiation damping functions to improve seismic response predictions of buried structures.

2.3 Time-Frequency Domains

In signal processing, two general approaches can be defined for solving systems of ordinary differential equations: Time domain analyses and Frequency-domain analyses.

The time-domain analysis begins with known conditions (velocities and displacements) at a specific moment and iteratively computes the conditions at each subsequent time step. Current time-stepping algorithms ensure accuracy, allowing the method to handle complex nonlinear models. However, this precision in the solution is only obtained if small time steps are taken in the analysis, causing long computation times. During the early stage of design, the time-domain analysis is too computationally expensive.

Instead, frequency-domain analyses are preferred in the initial design phase, offering faster calculations to accommodate frequent structural modifications. Obtained through transformations such as the Fourier Transform, the frequency domain doesn’t subdivide the time window into discrete time steps. This method assumed a finite length of T and then uses the property that any forcing term that is periodic in T can be split up into a summation of sinusoids.

2.4 Harmonic Balance Method

The Harmonic Balance Method (HBM) is an analytical technique for combining frequency domain analysis and nonlinearities. The fundamental principle of HBM is to assume that the solution to a nonlinear system can be represented as a finite sum of harmonic terms, each with an unknown amplitude and phase.

$$x(t) = A_0 + \sum_{n=1}^{N} A_n \cos(n\omega t) + B_n \sin(n\omega t)$$

Where A_0 is the DC component, A_n, B_n are the unknown Fourier coefficients for the harmonics and ω is the fundamental frequency. These unknowns are then determined by enforcing a balance of harmonics in the governing equations. The HBM is highly effective in analysing nonlinear vibrations [12], similar to the equations of motion of our system. Often, only the fundamental harmonic is retained, assuming it dominates system dynamics. This assumption breaks down in highly nonlinear cases [13].

An important assumption is made in this method that needs to be taken into consideration. The method is not suitable for transient dynamics since it assumes the system has already reached a periodic steady-state [14].

2.5 Resonant Column Test

The Resonant Column Test (RCT) is a geotechnical laboratory test designed to evaluate the dynamic properties of soils, particularly their shear modulus (G) and damping ratio (D) under small-strain conditions. This test simulates low-strain seismic wave propagation in soils and is widely used to determine the dynamic properties of the soil samples.

The test involves subjecting a cylindrical soil specimen to harmonic torsional, inducing resonance to determine the material’s dynamic response. The samples can be both hollow or full and usually have a height-to-width ratio of around two. The experiments with the hollow samples allow to record the radial strain too.

The apparatus consists of an oscillating top plate and a fixed bottom plate, positioned at the two extremities of the soil sample. The top plate is called the active plate, due to the presence of a motor that applies a torque to the system. The rotational response of the system is then recorded by accelerometers, positioned on the top plate. This accelerometer records the linear accelerations of the active plate, recorded at a radial distance of 5cm from the centre of the sample. This information will later be used to convert the accelerations from linear to angular, to match the simulated accelerations of the model.

The cross-sectional diagram of the entire apparatus used to evaluate the experimental results used in this research is presented in Figure 4.

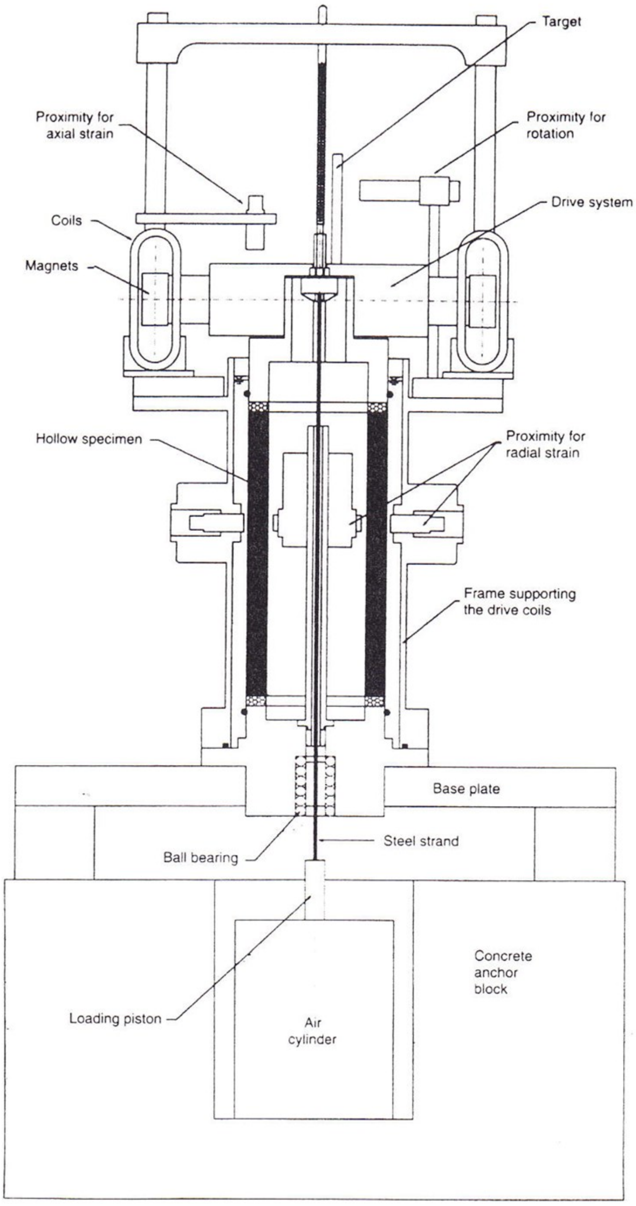

Figure 4 – Internal arrangement of the Resonant Column apparatus *[15]*

Chapter 3 – Modelling

This section outlines the models used to analyse the soil's response to dynamic forcing. The analysis begins with a linear model and subsequently incorporates the nonlinearities to develop the complete model. The models, previously presented in Van der Esch et al. [16], aim to replicate the Resonant Column Test, including its geometry, forcing, and boundary conditions, to enable comparison with experimental test data.

3.1 Geometry

Firstly, the geometry of the soil in the model and the reference system must be outlined. Since the soil samples examined in the RC test are saturated solid or hollow cylindrical specimens [17], the geometry in the model should be the same. In order to describe the entire 3D shape without the need for approximations, the geometry of the soil is defined with a cylindrical reference system. Each point is described through the three dimensions;

- x – The axial coordinate
- r – The radial distance from the centre of the specimen
- ϑ – The angle of rotation of horizontal cross-sections

To simplify the analysis, the specimen is modelled as a one-dimensional torsional beam. Given the axisymmetry of the specimen and of the forcing, the response is uniform in the azimuthal direction. This reduces the two-dimensional problem to a 1D model, with the response resulting dependent only on the axial coordinate and no radial variation.

Reducing the radial variable to a constant reduces complexity in subsequent derivations, as strain depends on r, as shown in the schematisation in Figure 5.

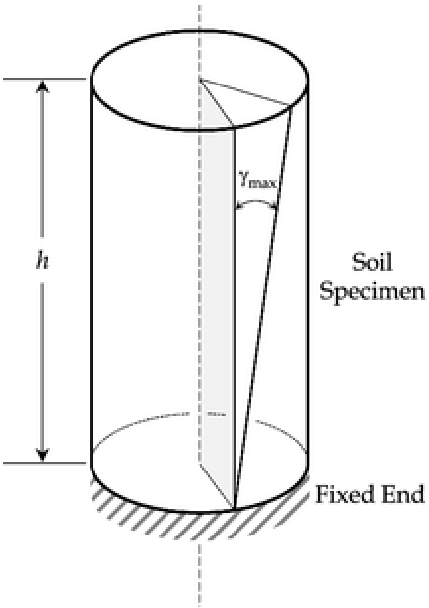

Figure 5 – Strain radius-dependency schematisation *[18]*

The small angle approximation is also used in the model to describe the displacement.

$$\Delta \approx r \cdot \theta \tag{1}$$

Therefore, the strain (γ) will be expressed as follows:

$$\gamma = \frac{\partial}{\partial x}\Delta \approx \mathrm{r}\frac{\partial \theta}{\partial x} \tag{2}$$

In order to obtain a representative measure of strain valid for the entire cross-section, it is necessary to select an appropriate radius. According to Drnevich et al. [19], an accepted range for this radius lies between 0.66 and 0.8 times the total radius of the soil sample. Another research performed by Chen and Stokoe [20] shows that the representative radius ranges from 0.76 to 0.82 for hyperbolic soil models. In this research, this representative radius will taken equal to 0.6 times the radius of the soil sample and for ease will be named the observation radius r_{obs}.

If the observation radius were to be set to zero, the resulting strain would also be zero. Consequently, selecting this radius as the representative value would yield a linear model, which is not desirable in this context. On the other hand, selecting the maximum radius could lead to an overestimation of nonlinearity. Therefore, an intermediate value is chosen, allowing for calibration as needed (a consideration that is further elaborated in Section 5.3).

3.2 Linear Model

3.2.1 Model Formulation

The mathematical derivation begins with a wave equation applied to a Kelvin-Voigt viscoelastic material [21]. This equation expresses the displacement, more specifically the horizontal rotation of the specimen θ, as a function of both space and time.

The Kelvin-Voigt viscoelastic relation models the material with a parallel configuration of a spring and dashpot. The spring and dashpot components account for the elastic and viscous responses, respectively. Their viscoelastic behaviour is characterized by two coefficients: η, representing viscosity, and G, representing the elastic modulus. By definition, the Kelvin-Voigt viscoelastic model expresses the total stress as the algebraic sum of the stress in each of the 2 components.

$$\rho \cdot \frac{\partial^2}{\partial t^2}\big(\theta(x,t)\big) = \frac{\partial^3}{\partial t \partial x^2}\big(\eta \cdot \theta(x,t)\big) + \frac{\partial^2}{\partial x^2}\big(G \cdot \theta(x,t)\big) \tag{3}$$

Where ρ is the cross-sectional soil density.

In the linear model, the shear modulus (G) is assumed to be constant and is assigned the value corresponding to the maximum strain, which reflects the conditions at the apex of the amplitude-frequency curve. This selection of G, rather than applying G_0, was implemented to more accurately replicate the conditions at the peaks, focusing on the central behaviour of the curve rather than the extremes.

The model incorporates hysteretic damping, ensuring that the damping term remains independent of the excitation frequency Ω. The damping coefficient η is defined as a function of the damping ratio ζ and the shear modulus through the following equation:

$$\eta = \frac{2 \cdot \zeta \cdot G}{\Omega} \tag{4}$$

Since in the linear model both the shear modulus and the damping are assumed to be constant in time and space, the equation is simplified to:

$$\rho \cdot \frac{\partial^2}{\partial t^2}\big(\theta(x,t)\big) = G \cdot \frac{\partial^2}{\partial x^2}\big(\theta(x,t)\big) + \eta \cdot \frac{\partial^3}{\partial t \partial x^2}\big(\theta(x,t)\big) \tag{5}$$

In the steady-state solution, the frequency of response of the soil sample will match the forcing frequency. Since the system is stimulated by harmonic excitation at Ω frequency, the steady-state solution is expressed in the following form.

$$\theta(x,t) = \mathrm{Re}\big(\hat{\theta}(x) \cdot e^{i\Omega t}\big) \tag{6}$$

The steady-state solution is introduced into the equation of motion. After the necessary simplifications, the equation describing the behaviour of the soil specimen is reduced to a second-order ordinary differential equation.

$$-\rho\Omega^2\hat{\theta}(x)e^{i\Omega t} = G\frac{\partial^2}{\partial x^2}\hat{\theta}(x)e^{i\Omega t} + i\Omega\eta\frac{\partial^2}{\partial x^2}\hat{\theta}(x)e^{i\Omega t} \tag{7}$$

$$\frac{\partial^2}{\partial x^2}\,\hat{\theta}(x) + \frac{\rho\Omega^2}{\{G + i\Omega\eta\}}\hat{\theta}(x) = 0 \tag{8}$$

In this simplified form, the variable $\hat{\theta}$ is a function solely dependent on spatial coordinates. This transformation allows the differential equation to be solved analytically by assuming the solution as a harmonic wave with wavenumber λ, as follows:

$$\hat{\theta}(x) = C \cdot e^{-i\lambda x} \tag{9}$$

$$\frac{\partial^2}{\partial x^2}\,C \cdot e^{-i\lambda x} + \frac{\rho\Omega^2}{\{G + i\Omega\eta\}}C \cdot e^{-i\lambda x} = 0 \tag{10}$$

$$-\lambda^2 + \frac{\rho\Omega^2}{\{G + i\Omega\eta\}} = 0 \tag{11}$$

$$\lambda_{1,2} = \pm\sqrt{\frac{\rho\Omega^2}{\{G + i\Omega\eta\}}} \tag{12}$$

$$\hat{\theta}(x) = C_1 \cdot e^{-i\lambda_1 x} + C_2 \cdot e^{-i\lambda_2 x} \tag{13}$$

3.2.2 Boundary Conditions

The equation contains two unknown coefficients, C_1 and C_2, requiring two equations to solve the system. These equations are determined using the boundary conditions at the specimen's two extremities. The specimen's boundary conditions are modelled to replicate those imposed by the Resonant Column Test's apparatus. The fixed-base and the free-top are labelled respectively the passive and the active ends. The schematisation of the two boundary conditions is represented in Figure 6.

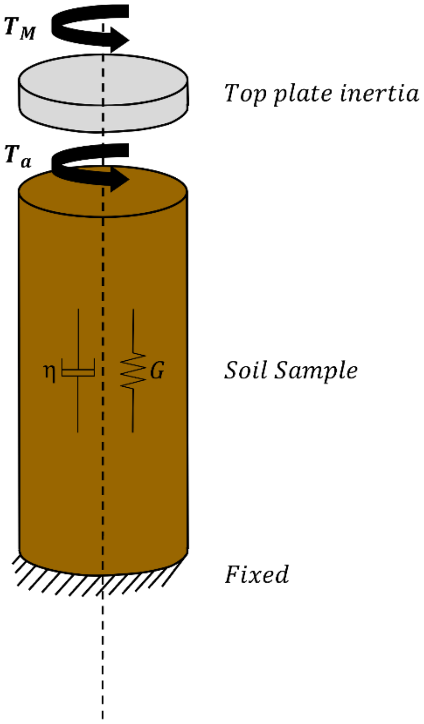

Figure 6 – Schematization of the boundary conditions

The two equations describing the boundary conditions are found through the equilibrium of forces at the two respective points of interest.

1. At $x = 0$, the passive end is a fixed plate, where all displacements and velocities are always zero.

$$\theta(0,t) = 0 \tag{14}$$

2. At $x = L$, the active end is influenced by the dynamic forcing of the motor. The motor directly applies the driving rotational force to the upper side of the plate of the RCT apparatus, with the soil specimen in contact on the lower side. The motor applies a sinusoidal torque of amplitude T_0 to the system, with a maximum drive of $1\ Nm$.

$$T_M = T_0 \cos(\Omega t) \tag{15}$$

This apparatus configuration allows the plate to rotate freely, with its inertia contributing to the equilibrium equation.

$$I_{active} + T_s = T_M \tag{16}$$

The active plate’s inertial contribution I_{active} is calculated as follows:

$$I_{active} = -\Omega^2 \cdot J_a \cdot \theta \tag{17}$$

Where Ja is the active plate’s polar mass moment of inertia.

The torque along the specimen, T_s, is given by the expression:

$$T_s(x,t) = \frac{Ip}{r} \cdot \sigma(x,t) \tag{18}$$

Where σ is the stress, estimated with the Kelvin-Voigt viscoelastic relation model as described in Section 3.2.1. The polar area moment of inertia (Ip) is calculated through Equation 19, as a function of the specimen polar mass moment of inertia Js.

$$Ip = \frac{Js}{\rho L} \tag{19}$$

$$T_s(x,t) = \frac{Js}{\rho L}\left(\frac{\partial}{\partial x}\theta(x,t)\right)(G + i\Omega\eta) \tag{20}$$

Combing all the abovementioned equations, the active end boundary condition is expressed through:

$$-\Omega^2 \cdot J_a \cdot \theta(L,t) + \frac{Js}{\rho L}\left(\frac{\partial}{\partial x}\theta(L,t)\right)(G + i\Omega\eta) = T_0 \cos(\Omega t) \tag{21}$$

3.3 Non-linear model

3.3.1 Model Formulation

Similarly to the linear model, the mathematical derivation begins with the wave equation, where θ, a function of both space and time, represents the rotation of the specimen. The difference with the linear model lies in the strain-dependent shear modulus. In the nonlinear model, the constitutive relation is no longer a constant but varies as the strain increases. This gives rise to an extra term inside the equation of motion compared to the linear model.

$$\rho \frac{\partial^2}{\partial t^2}(\theta) = \frac{\partial}{\partial x}(G) \cdot \frac{\partial}{\partial \mathrm{x}}(\theta) + G \cdot \frac{\partial^2}{\partial \mathrm{x}^2}(\theta) + \eta \cdot \frac{\partial^3}{\partial t \partial \mathrm{x}^2}(\theta) \tag{22}$$

The hyperbolic soil model is a nonlinear constitutive model, employed to describe this behaviour mathematically. The model assumes that the soil stiffness decreases with increasing strain but at a decreasing rate. The hyperbolic model is often used to represent the nonlinear behaviour of soils under small to moderate strains, where the soil behaviour is not highly nonlinear, resulting in slight inaccuracies at larger strain levels. The hyperbolic model is defined by the following equation [22]:

$$G = \frac{G_0}{1 + \left(\frac{\gamma}{\gamma_{ref}}\right)^{\beta}} \tag{23}$$

where G is the soil shear stiffness, γ is the strain, G_0 is the initial soil stiffness, γ_{ref} is the reference strain, and β is a decay constant that controls the rate of stiffness reduction with increasing strain.

$$\rho \frac{\partial^2}{\partial t^2}(\theta) = \frac{\partial}{\partial x}\left(\frac{G_0}{1 + \left(\frac{r \frac{\partial \theta}{\partial x}}{\gamma_{ref}} \right)^{\beta}} \right) \cdot \frac{\partial}{\partial \mathrm{x}}(\theta) + \frac{G_0}{1 + \left(\frac{r \frac{\partial \theta}{\partial x}}{\gamma_{ref}} \right)^{\beta}} \cdot \frac{\partial^2}{\partial \mathrm{x}^2}(\theta) + \eta \cdot \frac{\partial^3}{\partial t \partial \mathrm{x}^2}(\theta) \tag{24}$$

The harmonic balance method is an effective tool for analysing and solving nonlinear differential equations, especially if one is interested in the steady-state response. The periodic functions are expressed as a Fourier series, a sum of sine and cosine terms with varying frequencies. The contribution of higher-order harmonics to the overall solution diminishes progressively, making their inclusion less impactful. Throughout this study, the adopted solution contains the first three odd harmonics, as they provide sufficient accuracy, rendering higher-order terms unnecessary.

$$\theta(x,t) = \begin{matrix} \mathrm{U}_{C1}(x)\cos(1\Omega t) + \mathrm{U}_{S1}(x)\sin(1\Omega t) + \\ \mathrm{U}_{C3}(x)\cos(3\Omega t) + \mathrm{U}_{S3}(x)\sin(3\Omega t) + \\ \mathrm{U}_{C5}(x)\cos(5\Omega t) + \mathrm{U}_{S5}(x)\sin(5\Omega t) \ldots \end{matrix} \tag{25}$$

In Equation 25, the cosine and sine components are scaled by their respective amplitude coefficients. The subscripts of these coefficients indicate the harmonic number and the corresponding sinusoidal component. These coefficients are functions of the spatial coordinate x.

The solution of the differential equation (Eq. 25) is substituted back into Equation 24, resulting in a complicated expression that is difficult to solve directly. This equation contains too many variables, given rise by the partial derivations of the multiple harmonic components to be solved analytically. However, this expression can be decomposed into a system of six equations, each corresponding to a specific harmonic. This decomposition is performed through the orthogonality property of sinusoidal functions in integration. By definition, the integral of the product of two orthogonal functions over a specific range is zero. If $f(x)$ and $g(x)$ are orthogonal over the interval $[a, b]$, then:

$$\int_a^b f(x) \cdot g(x)\, dx = 0 \tag{26}$$

In our application, the interval is equal to the period, represented by the following expression:

$$T = \frac{2\pi}{\Omega} \tag{27}$$

The solution is hence projected onto each harmonic by integrating the equation with the associated sinusoidal term. This mathematical procedure is repeated for all 6 sinusoids, giving rise to a system of 6 equations.

$$\frac{-\rho\Omega^2}{G_0}\frac{\partial^2}{\partial t^2}\left(\mathrm{U}_{C1}(x)\right) = \alpha \cdot \frac{\partial^2}{\partial \mathrm{x}^2}\left(\mathrm{U}_{C1}(x)\right) + 2 \cdot \zeta \cdot \frac{\partial^3}{\partial t \partial \mathrm{x}^2}\left(\mathrm{U}_{S1}(x)\right) \tag{28}$$

$$\frac{-\rho\Omega^2}{G_0}\frac{\partial^2}{\partial t^2}\left(\mathrm{U}_{S1}(x)\right) = \alpha \cdot \frac{\partial^2}{\partial \mathrm{x}^2}\left(\mathrm{U}_{S1}(x)\right) - 2 \cdot \zeta \cdot \frac{\partial^3}{\partial t \partial \mathrm{x}^2}\left(\mathrm{U}_{C1}(x)\right) \tag{29}$$

$$\frac{-9\rho\Omega^2}{G_0}\frac{\partial^2}{\partial t^2}\left(\mathrm{U}_{C3}(x)\right) = \alpha \cdot \frac{\partial^2}{\partial \mathrm{x}^2}\left(\mathrm{U}_{C3}(x)\right) + 6 \cdot \zeta \cdot \frac{\partial^3}{\partial t \partial \mathrm{x}^2}\left(\mathrm{U}_{S3}(x)\right) \tag{30}$$

$$\frac{-9\rho\Omega^2}{G_0}\frac{\partial^2}{\partial t^2}\left(\mathrm{U}_{S3}(x)\right) = \alpha \cdot \frac{\partial^2}{\partial \mathrm{x}^2}\left(\mathrm{U}_{S3}(x)\right) - 6 \cdot \zeta \cdot \frac{\partial^3}{\partial t \partial \mathrm{x}^2}\left(\mathrm{U}_{C3}(x)\right) \tag{31}$$

$$\frac{-25\rho\Omega^2}{G_0}\frac{\partial^2}{\partial t^2}\left(\mathrm{U}_{C5}(x)\right) = \alpha \cdot \frac{\partial^2}{\partial \mathrm{x}^2}\left(\mathrm{U}_{C5}(x)\right) + 10 \cdot \zeta \cdot \frac{\partial^3}{\partial t \partial \mathrm{x}^2}\left(\mathrm{U}_{S5}(x)\right) \tag{32}$$

$$\frac{-25\rho\Omega^2}{G_0}\frac{\partial^2}{\partial t^2}\left(\mathrm{U}_{S5}(x)\right) = \alpha \cdot \frac{\partial^2}{\partial \mathrm{x}^2}\left(\mathrm{U}_{S5}(x)\right) - 10 \cdot \zeta \cdot \frac{\partial^3}{\partial t \partial \mathrm{x}^2}\left(\mathrm{U}_{C5}(x)\right) \tag{33}$$

The system of 6 equations can be expressed in matrix form for easier visualisation.

$$\bar{\bar{R}} \cdot \bar{U} = \bar{\bar{M}} \cdot \overline{U''} \tag{34}$$

The matrix $\bar{\bar{M}}$ is calculated through the summation of matrixes $\overline{\overline{M_1}}$ and $\overline{\overline{M_2}}$.

$$\bar{\bar{M}} = \overline{\overline{M_1}} + \overline{\overline{M_2}} \tag{35}$$

$\overline{\overline{M_1}}$ is obtained by the multiplication of the 6x6 identity matrix and the term α.

$$\overline{\overline{M_1}} = I \times \alpha = \begin{bmatrix} 1 & 0 & 0 & 0 & 0 & 0 \\ 0 & 1 & 0 & 0 & 0 & 0 \\ 0 & 0 & 1 & 0 & 0 & 0 \\ 0 & 0 & 0 & 1 & 0 & 0 \\ 0 & 0 & 0 & 0 & 1 & 0 \\ 0 & 0 & 0 & 0 & 0 & 1 \end{bmatrix} \times \frac{1}{1 + \left(\frac{r\frac{\partial\theta}{\partial x}}{\gamma_{ref}}\right)^{\beta}} \cdot \left(1 - \frac{\beta \cdot G_0 \cdot \left(\frac{r\frac{\partial\theta}{\partial x}}{\gamma_{ref}}\right)^{\beta}}{1 + \left(\frac{r\frac{\partial\theta}{\partial x}}{\gamma_{ref}}\right)^{\beta}}\right) \tag{36}$$

All the other vectors and matrixes named in Equation 34 are reported below.

$$\bar{\bar{R}} = \begin{bmatrix} \frac{-\rho\Omega^2}{G_0} & 0 & 0 & 0 & 0 & 0 \\ 0 & \frac{-\rho\Omega^2}{G_0} & 0 & 0 & 0 & 0 \\ 0 & 0 & \frac{-9\rho\Omega^2}{G_0} & 0 & 0 & 0 \\ 0 & 0 & 0 & \frac{-9\rho\Omega^2}{G_0} & 0 & 0 \\ 0 & 0 & 0 & 0 & \frac{-25\rho\Omega^2}{G_0} & 0 \\ 0 & 0 & 0 & 0 & 0 & \frac{-25\rho\Omega^2}{G_0} \end{bmatrix}$$

$$\bar{U} = \begin{bmatrix} \mathrm{U}_{C1} \\ \mathrm{U}_{S1} \\ \mathrm{U}_{C3} \\ \mathrm{U}_{S3} \\ \mathrm{U}_{C5} \\ \mathrm{U}_{S5} \end{bmatrix} \qquad \overline{U''} = \begin{bmatrix} \mathrm{U''}_{C1} \\ \mathrm{U''}_{S1} \\ \mathrm{U''}_{C3} \\ \mathrm{U''}_{S3} \\ \mathrm{U''}_{C5} \\ \mathrm{U''}_{S5} \end{bmatrix} \qquad \overline{\overline{M_2}} = \begin{bmatrix} 0 & 2\zeta & 0 & 0 & 0 & 0 \\ -2\zeta & 0 & 0 & 0 & 0 & 0 \\ 0 & 0 & 0 & 6\zeta & 0 & 0 \\ 0 & 0 & -6\zeta & 0 & 0 & 0 \\ 0 & 0 & 0 & 0 & 0 & 10\zeta \\ 0 & 0 & 0 & 0 & -10\zeta & 0 \end{bmatrix}$$

The equations have no analytical solution and must be solved numerically. For this purpose, the Boundary Value Problem Fourth-order Method (Bvp4c) solver is used in MATLAB. This solver integrates a system of differential equations subject to boundary conditions with the help of an initial solution guess.

The solver discretises the spatial variable into numbers, independently varying the number of elements using an adaptive mesh refinement, to improve the solution accuracy. The solver obtains numerical solutions, with the demanded tolerances, for the required unknowns at each of the nodes. The absolute and relative tolerances of the solver are set equal to 10^{-9} and 10^{-6} respectively.

Nonlinear systems can have multiple equilibrium states, as shown graphically in Section 2.1. Consequently, we adopt two directions of frequency sweeping. The frequencies must be varied firstly from the minimum frequency to the maximum frequency and then repeated in the opposite direction. These solutions will be labelled as upwind and downwind respectively in the result sections 5.2.

3.3.2 Boundary Conditions

The boundary conditions are identical to the ones employed in the linear model described in Section 3.2.2. The solver can handle the dynamic boundary condition, enabling us to compare the two different models with each other.

Chapter 4 - Experimental Data

Experimental data is essential to validate the proposed models, aiming to demonstrate that the simulated response closely replicates real-life conditions observed in laboratory experiments.

4.1 Database description

In order to validate the models, the dataset described in Ciancimino et al. [23] is utilized. The database includes 252 soil samples collected from various locations across Italy over the past 30 years. These samples exhibit diverse granulometric characteristics and have been analysed through different laboratory tests performed in Politecnico di Torino and in Sapienza Università di Roma. For uniformity, only the samples analysed in Politecnico di Torino with RC test were taken into consideration. The RC tests were carried out using the free-fixed device of the geotechnical laboratory of PoliTo [17] [15]. The apparatus can perform both resonant column or cyclic torsional shear tests.

For each soil sample the following categories of information are provided:

- General information – contains the initial shear modulus (G_0)
- Physical properties – contains the soil density (ρ)
- RC Testing data – contains all the recordings of the RC apparatus, such as frequencies, torques, accelerations, etc.

Three different methods were used in the experiments to estimate the damping ratio: Half-power Bandwidth, Free Vibration Decay and Resonance Factor. As the other two methods have been proven inaccurate when the resonance curve bends (softening), the free vibration decay method has always been chosen for all samples for uniformity.

The free-vibration decay method is applied considering the 10 cycles of free-damped vibrations at the end of the loading cycles. By knowing two successive peak amplitudes z_n and z_{n+1}, the logarithmic decrement δ_{n+1} is computed as:

$$\delta_{n+1} = \ln\left(\frac{z_n}{z_{n+1}}\right) \tag{37}$$

The average value is used to compute the damping ratio as:

$$D = \frac{\delta}{2\pi} \tag{38}$$

This value is used in our model as the input for the damping ratio ζ in the models.

After all the considerations listed above, three samples were selected and their data was used to verify the model. The soil samples selected with the abovementioned criteria are PoliTo052, PoliTo024 and PoliTo020, respectively named Soil Sample 1, Soil Sample 2 and Soil Sample 3. The material properties and granulometry are reported in Table 1 to Table 3.

Soil Sample 1	**PoliTo052**		
Material properties			
Initial shear modulus	G_0	50,73	MPa
Soil density	ρ	2008,84	kg/m^3
Mean effective stress	p'	57,7	kPa
Granulometry			
Gravel [%]	3,6		
Sand [%]	36,2		
Silt [%]	39,6		
Clay [%]	20,5		

Table 1 – Soil Sample 1 granulometry and properties

Soil Sample 2	**PoliTo024**		
Material properties			
Initial shear modulus	G_0	124,04	MPa
Soil density	ρ	2103,67	kg/m^3
Mean effective stress	p'	168,1	kPa
Granulometry			
Gravel [%]	0,1		
Sand [%]	16,5		
Silt [%]	67,4		
Clay [%]	16,0		

Table 2 – Soil Sample 2 granulometry and properties

Soil Sample 3	**PoliTo020**		
Material properties			
Initial shear modulus	G_0	225,07	MPa
Soil density	ρ	2103,67	kg/m^3
Mean effective stress	p'	250,9	kPa
Granulometry			
Gravel [%]	1,0		
Sand [%]	56,4		
Silt [%]	30,9		
Clay [%]	11,7		

Table 3 – Soil Sample 3 granulometry and properties

The magnitude of acceleration of the experimental data is plotted versus the frequency of excitation in Figure 7 to Figure 9.

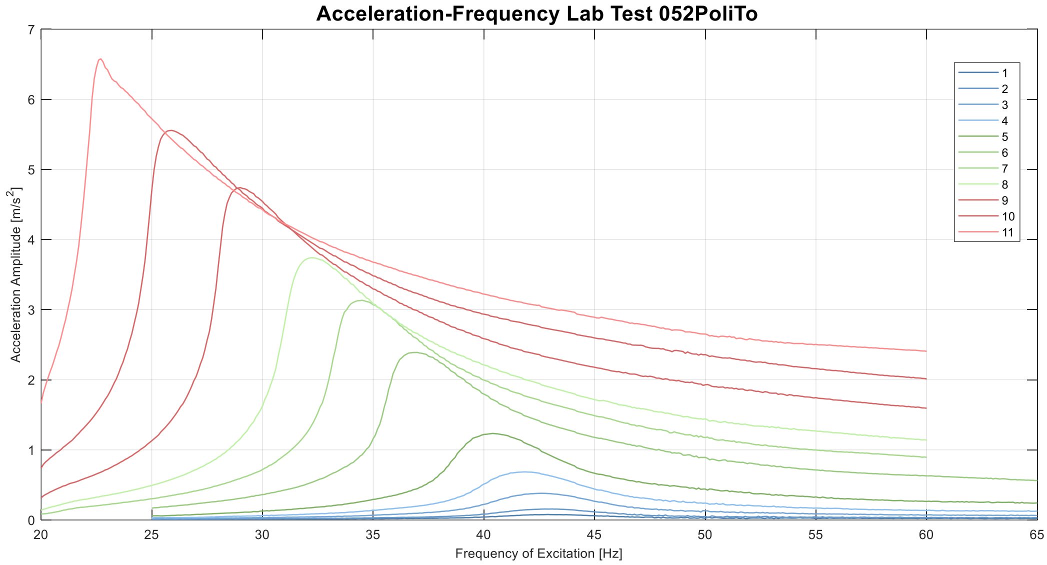

Figure 7 – Soil sample 1 experimental acceleration-frequency graph

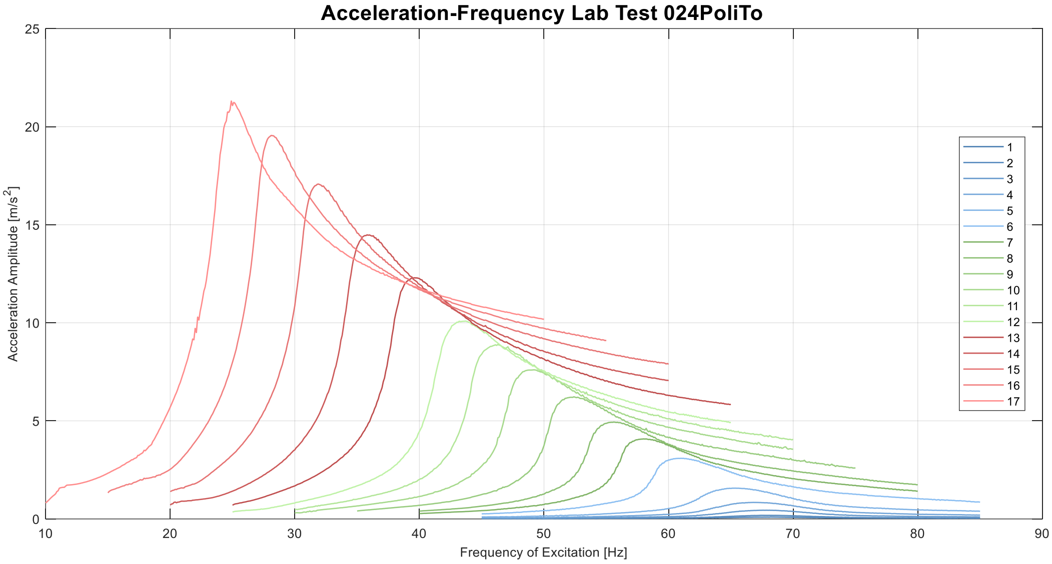

Figure 8 – Soil sample 2 experimental acceleration-frequency graph

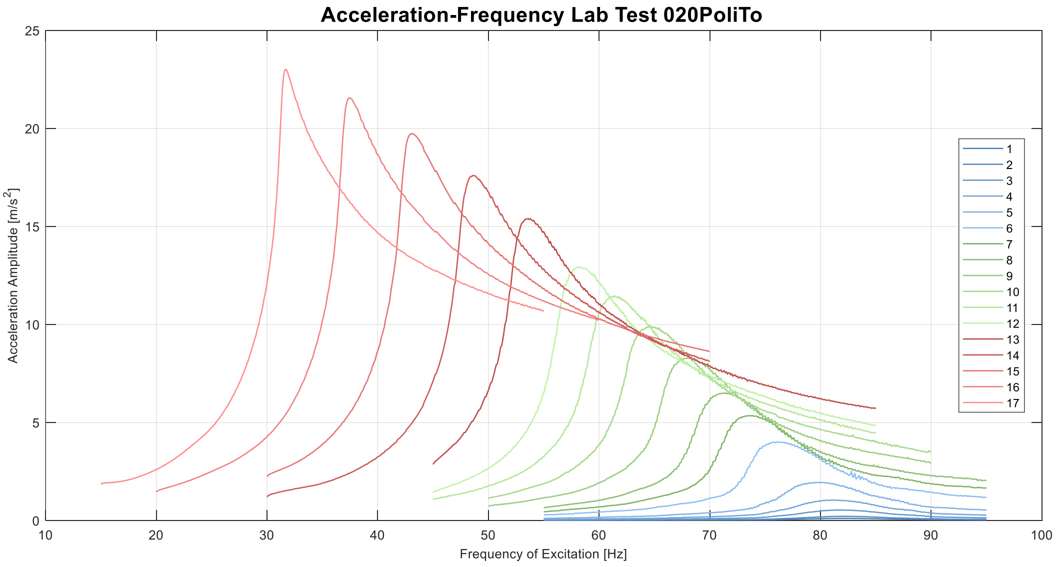

Figure 9 – Soil sample 3 experimental acceleration-frequency graph

4.2 Hyperbolic Soil Model Fitting

As previously mentioned in Section 3.3, the nonlinear model uses the hyperbolic soil model to numerically represent the shear modulus of the soil. This soil model must be calibrated by tunning the parameters γ_{ref} and β to match experimental data. The reference strain is defined as the value corresponding to 50% of the normalized shear modulus $\left(\frac{G}{G_0}\right)$ from the experimental curve, with β adjusted to match the stiffness reduction rate.

The hyperbolic soil models of the 3 different soil samples were calibrated with the parameters listed in Table 4 and their plots visualised in Figure 10 to Figure 12 respectively.

Soil Sample	$\boldsymbol{\gamma_{ref}}$ [%]	$\boldsymbol{\beta}$ [−]
1	0,000374	1,02
2	0,000278	0,98
3	0,000302	1,03

Table 4 – Hyperbolic Soil Model Parametric Calibration

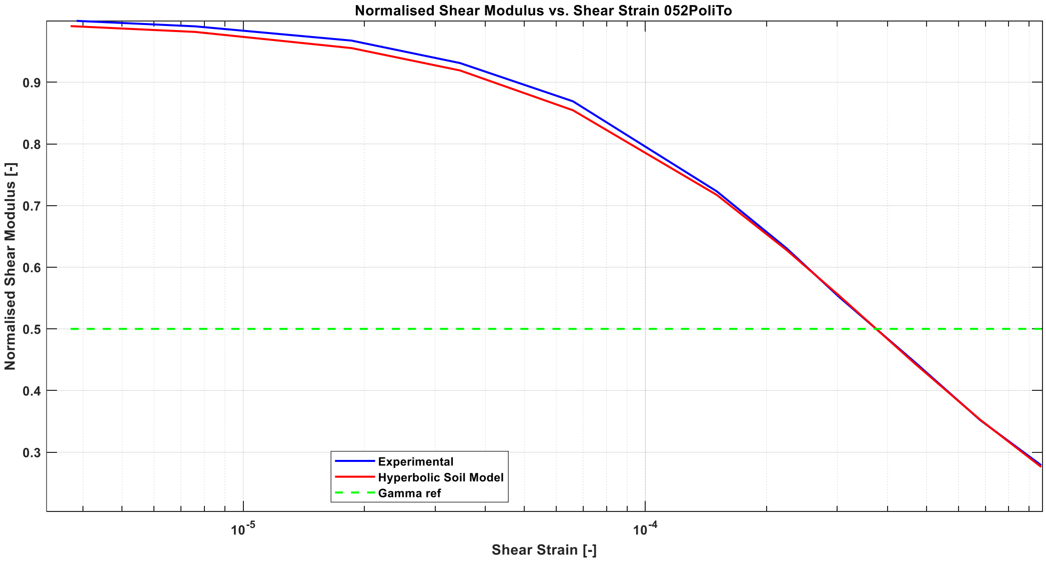

Figure 10 – Fitting of Hyperbolic Soil Model for Soil Sample 1

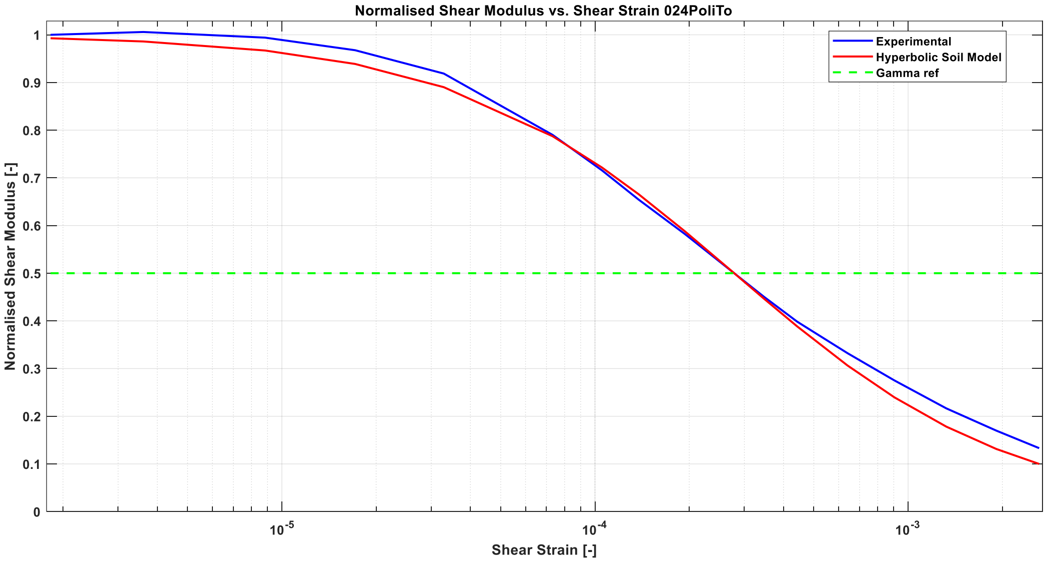

Figure 11 – Fitting of Hyperbolic Soil Model for Soil Sample 2

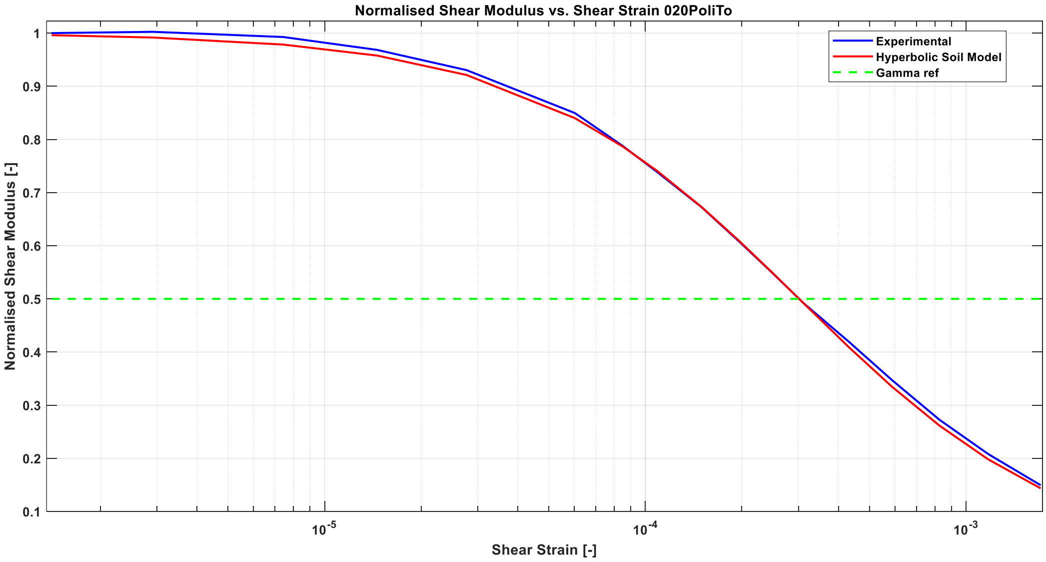

Figure 12 – Fitting of Hyperbolic Soil Model for Soil Sample 3

4.3 Experimental torque values

The database provided by Ciancimino et al. [23], containing the experimental torque values, provides the necessary input for our model. The data of the torque applied by the motor is presented in the form of a torque sequence recorded over time. The motor can apply, under loading control, sinusoidal loading torques with a maximum amplitude of 1 Nm.

Each loading sequence is divided into three steps: an initial null force, followed by the sinusoidal forcing and terminated with another null force period to allow the free decay of the vibrations. An example of a loading sequence is presented in Figure 13. The maximum amplitude of the torque is taken as the value of T_0.

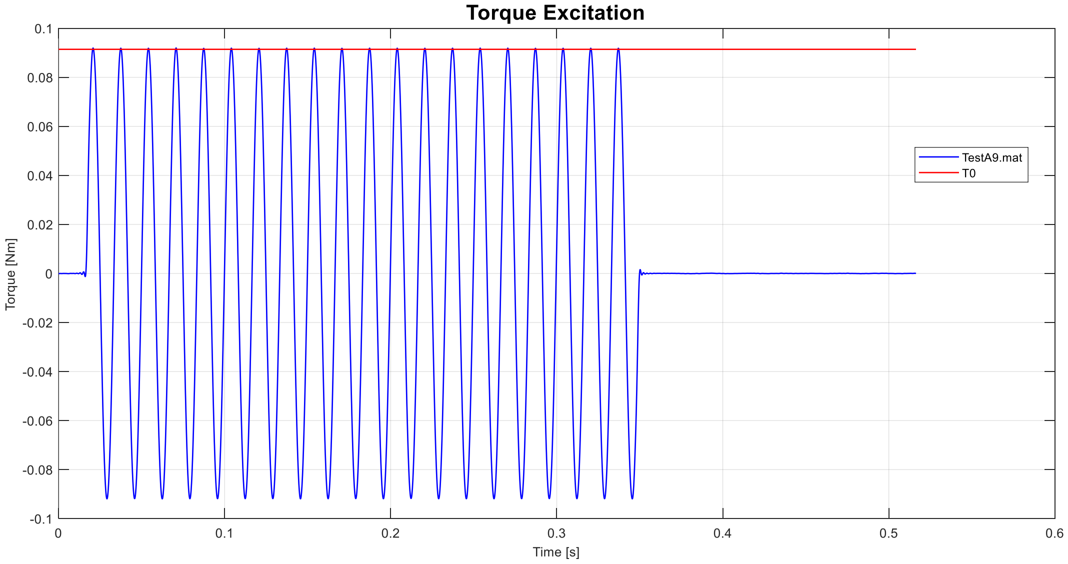

Figure 13 – RCT Torque excitation for Test 9

4.4 Experimental steady-state accelerations

The accelerometer is positioned at the height of the top plate, at a horizontal distance of 5 cm from the soil sample's centre. It records the linear accelerations performed by the rotating top plate.

The experimental accelerometer readings are recorded and plotted against time. Following the torque loading steps described earlier, the acceleration data exhibits three distinct phases: transient response, steady-state response, and free decay. The analysis focuses on extracting the steady-state solution to compare with numerical results, as the model emphasizes this phase.

To achieve this for all torque loadings and all frequency steps, a custom code was developed. The code calculates the average of all positive and negative peaks within the middle section of the graph, thereby excluding the transient and free decay phases. Averaging both peaks minimizes errors caused by non-zero-centred accelerations. This may arise due to certain soil mechanics phenomena, such as ratcheting. The positive and negative peak averages are illustrated by the dotted red line in Figure 14.

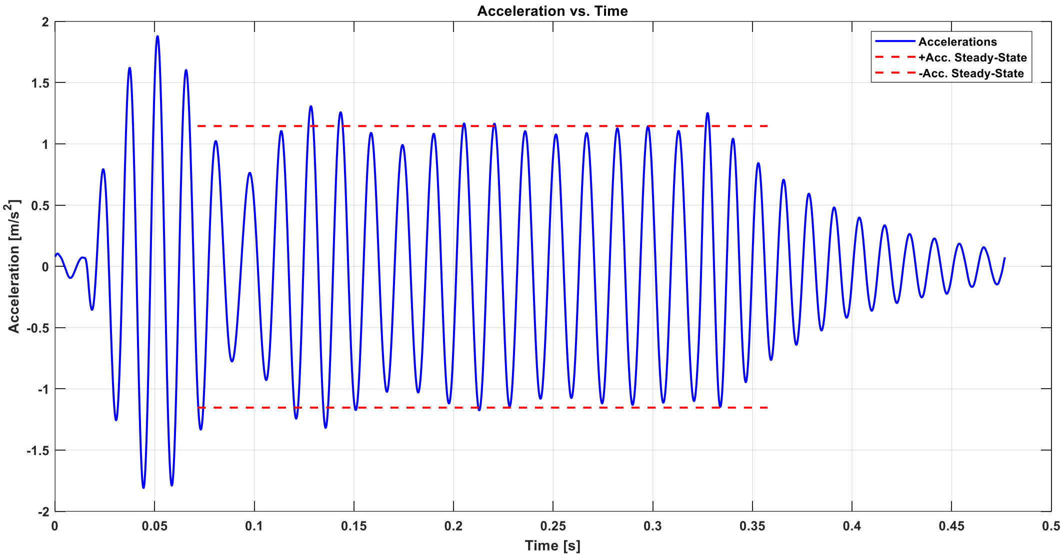

Figure 14 – Acceleration time history and positive/negative average acceleration values at steady state

The steady-state solution, in Figure 15, is obtained by the mean of the absolute values of the positive and negative peak averages.

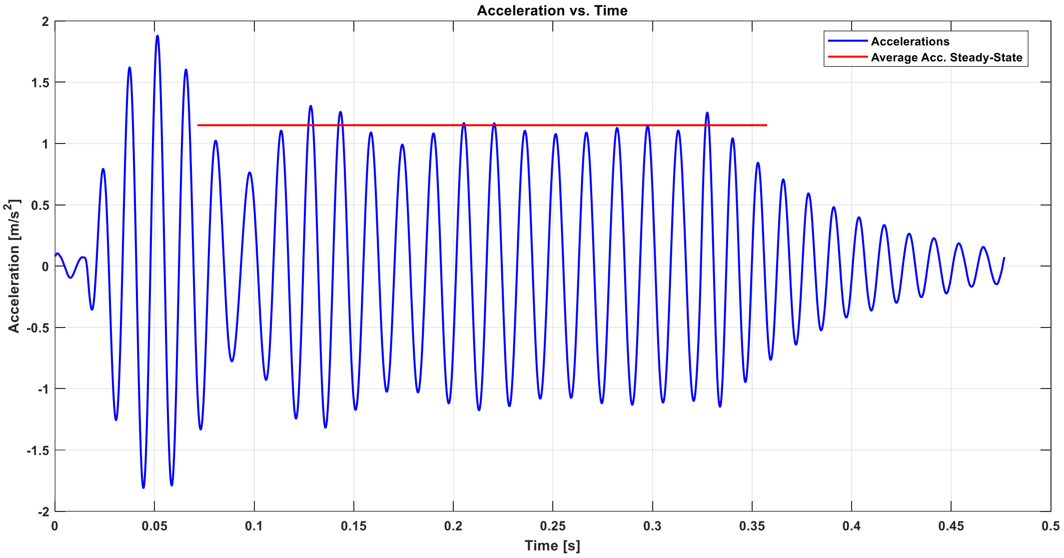

Figure 15 - Steady-state solution of test 7 frequency 101

The procedure must be adaptable to extract the steady-state solution across all frequency steps for each torque loading, regardless of variations in amplitude, shape, or time span of the acceleration recordings. Two additional examples are shown in Figure 16 and Figure 17.

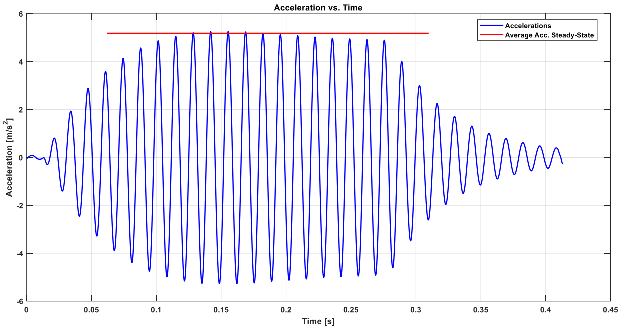

Figure 16 – Steady-state solution of test 7 frequency 201

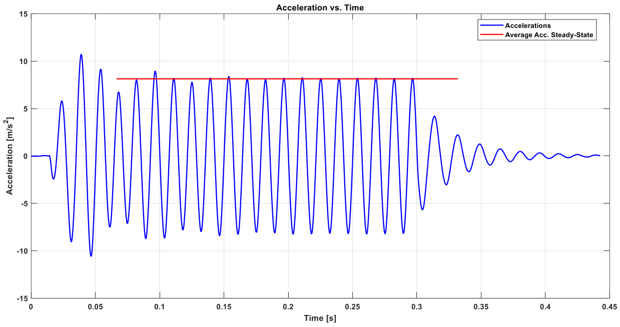

Figure 17 – Steady-state solution of test 14 frequency 401

4.5 Model Performance metrics

Since the experimental soil conditions at the resonance peak are reported for each loading step, it is possible to compare these values with the simulated conditions generated by the different models. To perform this verification, the values of strain (γ) and shear modulus (G) obtained from the experiments are compared with those predicted by the model. A percentage difference between the experimental and modelled values is then calculated to assess the accuracy of the assumed torque and ensure the validity of the model.

The two parameters mentioned are calculated with the following equations, where γ_{model} is the strain simulated by the model at the top boundary condition and γ_{data} is the resonance strain value presented in the database.

$$\gamma_{error} = \frac{\max(\mathrm{\gamma_{model}}) - \gamma_{data}}{\gamma_{data}} \tag{39}$$

$$G_{error} = \frac{\min(\mathrm{G_{model}}) - G_{data}}{G_{data}} \tag{40}$$

Chapter 5 – Results

The results of the model will be presented in this section. After discussing the contribution of the super-harmonics, we examine the amplitude of accelerations of the models' solutions and compare them with the experimental data obtained through the RC lab tests.

5.1 Contribution of super-harmonics

As outlined in Equation 32, the Harmonic Balance Method solves the equation of motion for the nonlinear model by decomposing the solution into individual harmonics. In contrast, the experimental solution represents the total signal, containing all harmonics. Therefore, when comparing the model's numerical solution to the experimental data, it is crucial to evaluate the contribution of the higher-order harmonics. If their contribution is negligible compared to the first harmonic, they can be disregarded, allowing the amplitude of the first harmonic to be compared directly to the experimental total signal.

In Figure 18, the amplitudes of acceleration of the first three odd harmonics are plotted against the excitation frequency for a low-strain simulation. In this plot, the nonlinear upwind and downwind solutions are overlapped to outline any possible differences.

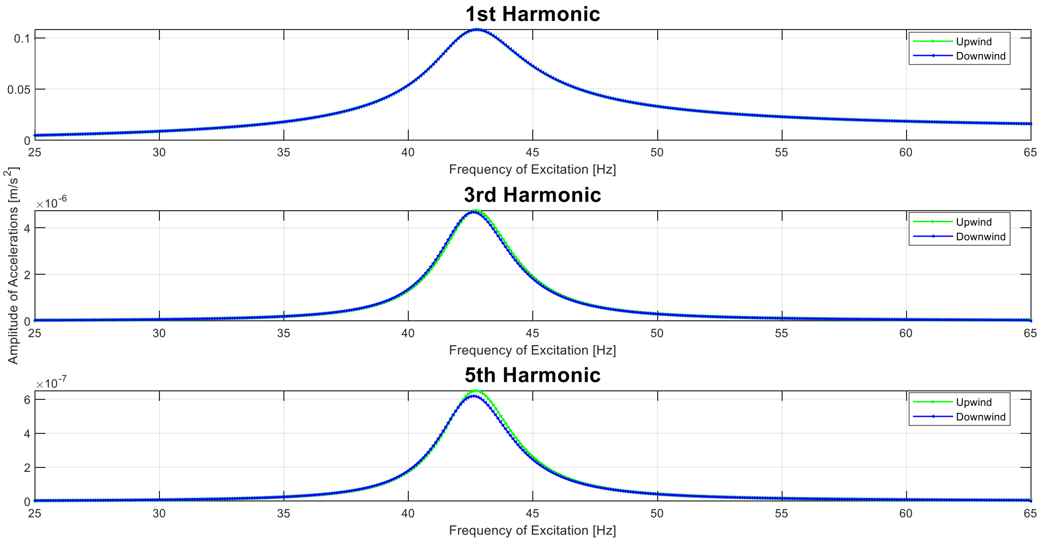

Figure 18 – The acceleration amplitude vs excitation frequency obtained using the nonlinear model for which a low external torque is applied corresponding to a low-strain state

As expected, the amplitude of the accelerations decreases with an increasing harmonic number. From this plot, it is evident that the contribution of the 3rd and 5th harmonics are four orders of magnitude lower than the 1st harmonic, concluding that the super-harmonics may be neglected. Secondly, a slight difference between the upwind and downwind solutions can be observed. At such low-strain levels, this discrepancy is not expected, as the nonlinearities are insufficient to cause significant differences. Nonlinear effects become more pronounced at higher strain levels, where the amplitude curve exhibits a characteristic leftward bend, and the solutions diverge. Thus, these inaccuracies are likely due to numerical errors in the solver.

The same study is repeated for a medium-strain test and illustrated in Figure 19. In this latter test, the contribution of the super-harmonics is still negligible, however, now the amplitudes are two orders of magnitude lower. As expected, at these strain levels, the solutions of the upwind and downwind start to diverge from each other in correspondence with the curve's peak.

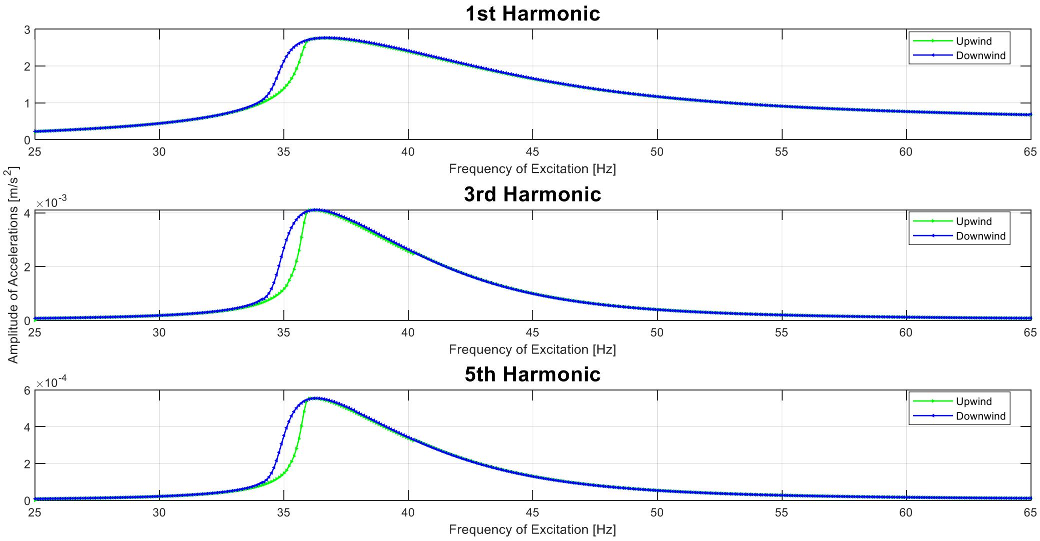

Figure 19 – The acceleration amplitude vs excitation frequency obtained using the nonlinear model for which a medium external torque is applied corresponding to a medium-strain state

After comparing the high-strain test's results, illustrated in Figure 20, it is possible to observe the same trend. The higher the strain in the simulation, the higher the contribution of the 3rd and 5th harmonics. These findings are attributed to the nonlinearities of the model, which are captured by the higher-order harmonics. Consequently, their contribution increases as the strain grows, becoming influential in high-strain tests.

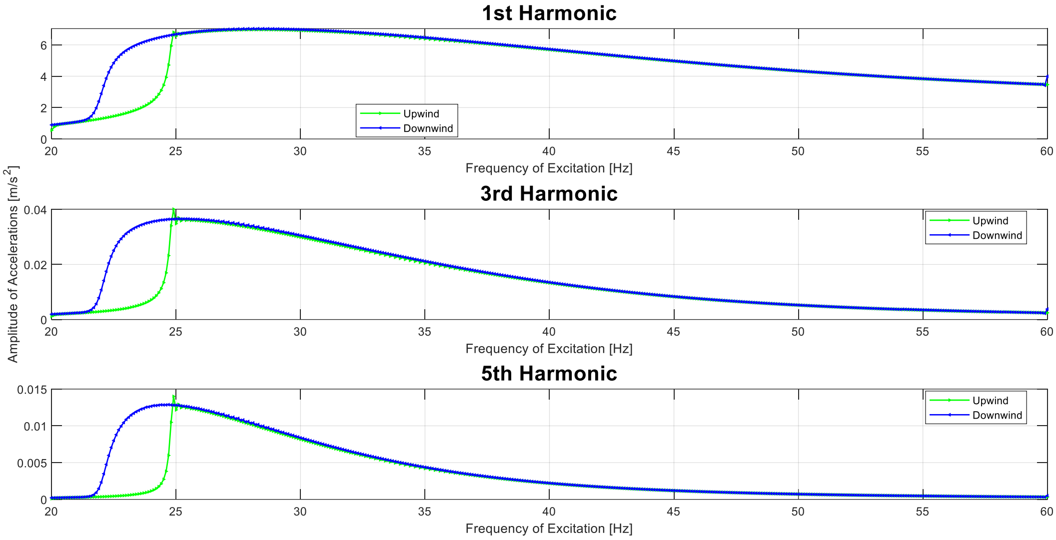

Figure 20 – The acceleration amplitude vs excitation frequency obtained using the nonlinear model for which a high external torque is applied corresponding to a high-strain state

From this analysis, it can be concluded that the amplitudes of the super-harmonics are orders of magnitude smaller than those of the first harmonic, rendering them negligible. To further validate this for high-strain levels, the numerical total signal is constructed and compared with the amplitude of the first harmonic, illustrated in Figure 21. The acceleration magnitude of the total signal closely overlaps with the first harmonic’s response, confirming that super-harmonics can be neglected for simplification.

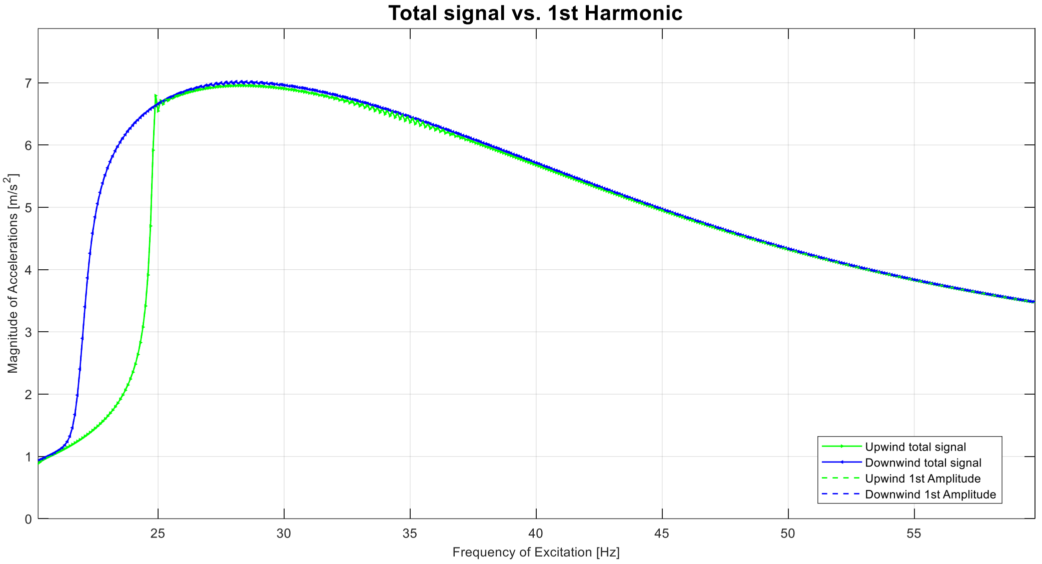

Figure 21 – Comparison of the amplitude of acceleration of the 1st harmonic vs the magnitude of acceleration of the total signal obtained using the nonlinear model

For future comparative analyses between the nonlinear numerical solution and the experimental total signal, it is acceptable to disregard the third and fifth harmonics.

5.2 Linear vs Nonlinear Models Comparison

The divergence between the linear and nonlinear numerical models was examined to evaluate the importance and correct implementation of material nonlinearity.

First, to verify the correct application of the hyperbolic soil model, the reference strain γ_{ref} is significantly increased. As γ_{ref} approaches infinity, the two models should converge, confirming the model's consistency.

After simulating the response of Soil Sample 1 with the aid of both linear and nonlinear models, the amplitude of acceleration was plotted against the frequency of excitation. All 11 loading steps conducted on this sample were assessed, with Test 1 corresponding to the lowest applied torque and Test 11 to the highest. For comparison purposes, only three of the eleven tests are presented in this report: one at low strain, one at medium strain, and one at high strain, labelled Figure 22 to Figure 24.

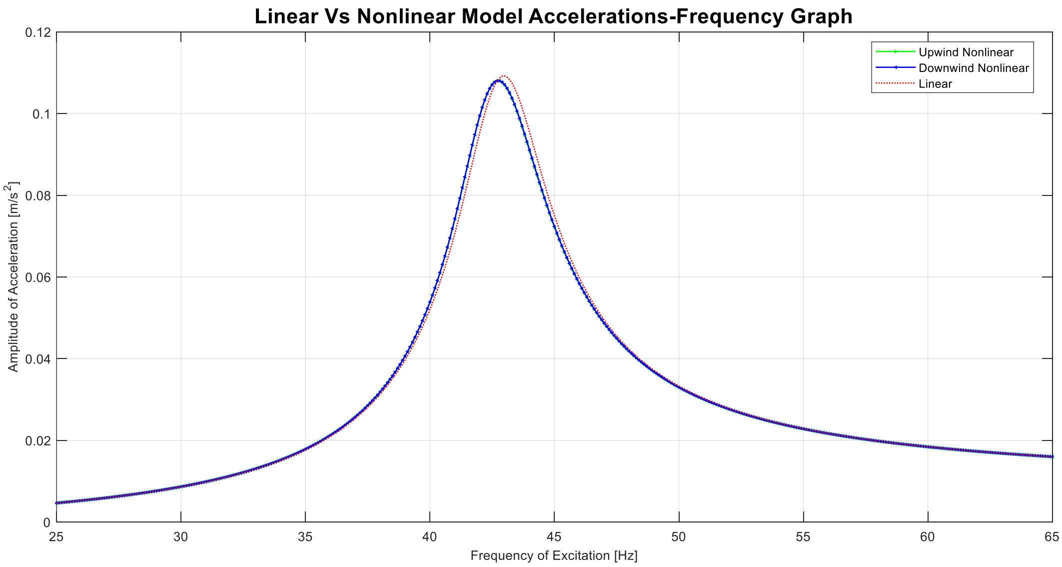

Figure 22 – Soil Sample 1 Linear vs nonlinear model comparison corresponding to the low-strain state

At low-strain levels, the nonlinear model's solution closely resembles the linear one. This is because the shear modulus remains near G_0, leading to minimal contributions from nonlinearities in the solution.

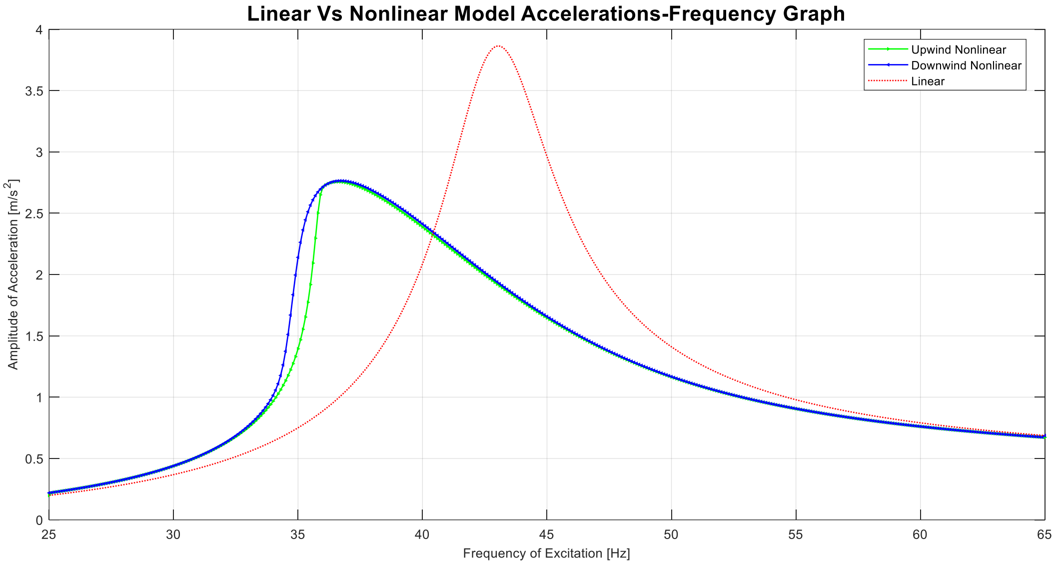

Figure 23 – Soil Sample 1 Linear vs nonlinear model comparison corresponding to the medium-strain state

As the strain in the soil sample increases, the linear and nonlinear solutions begin to diverge. With higher applied torque, the amplitude of the linear response increases, but the resonance peak remains fixed at the same frequency. Conversely, the nonlinear solution exhibits a resonance shift.

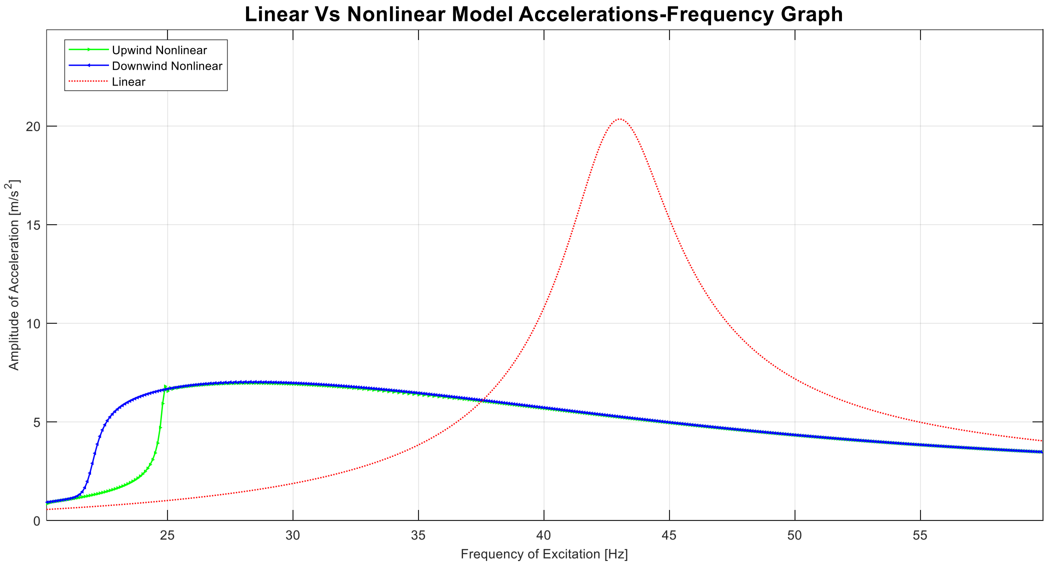

Figure 24 – Soil Sample 1 Linear vs nonlinear model comparison corresponding to the high-strain state

The same behaviour described in the medium-strain state can be observed in the high-strain state, but with greater emphasis. The discrepancy between the two models increases with higher torque levels, as greater torque induces higher strain and amplifies soil nonlinearities, which are captured only by the nonlinear model.

From this comparison analysis, it is possible to conclude that the linear fails to account for the apparent soil softening observed experimentally, while the nonlinear model successfully tracks the shift in peak frequency. This enables us to verify the implementation of the hyperbolic soil model.

5.3 Nonlinear Model Simulations vs Experimental Results

In this subsection, the solution of the nonlinear numerical model will be compared to the experimental signal found through the Resonant Column Tests. A plot for each of the three strain states (low, medium and high), presented in Figure 25 to Figure 27, is examined.

The analysis of the presented graphs indicates that the proposed nonlinear model effectively reproduces the experimental results obtained from the RCT. The solutions derived from the numerical simulations exhibit a good agreement with the laboratory data across most frequencies and strain states.

Furthermore, by employing both upwind and downwind solutions, the model accurately captures the shift in resonance towards lower frequencies as the amplitude increases. This is evidenced by the fact that the experimental response remains bounded within the two frequency sweep curves.

The overall shape of the response is well replicated for small and medium strain levels. The inflection points of the curves and the peaks are observed at comparable frequencies, yielding similar overall shapes. However, this is not valid for higher strain states, where discrepancies emerge. The shape of the response curve in the high-strain case demonstrates deviations from the experimental one. In particular, the simulated response appears excessively damped, particularly on the right side of the resonance peak.

Despite these promising results, certain inaccuracies persist in the model, highlighting areas for further refinement. The model consistently overestimates the acceleration amplitude near resonance, with the simulated responses exhibiting higher magnitudes than those recorded in the experimental tests across all strain states. However, the extent of this overestimation diminishes as strain increases, leading to a reduction in the relative error. In other words, the discrepancy between experimental and numerical results decreases when considered in relation to the overall signal amplitude as strain levels increase.

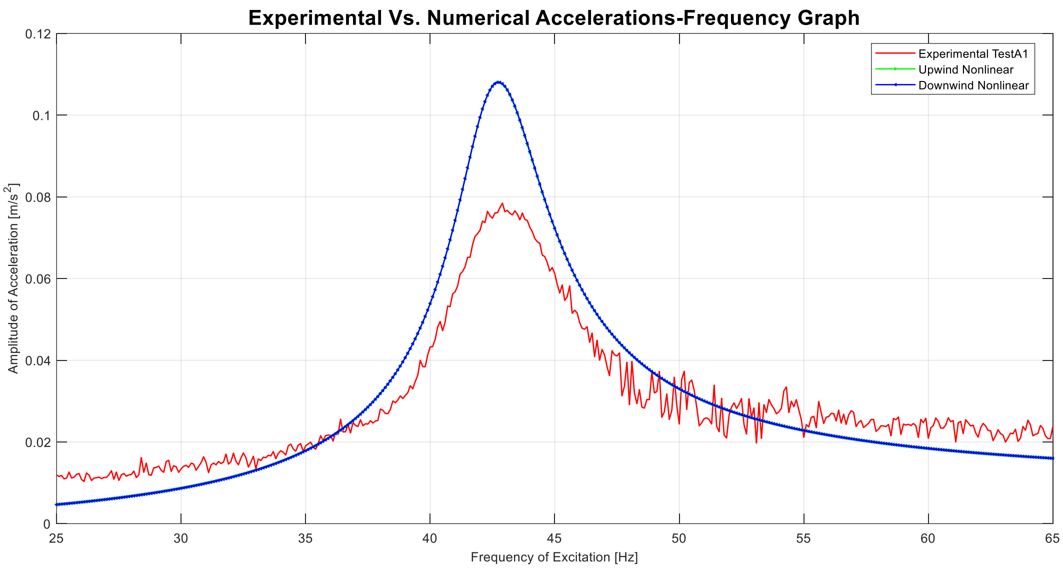

Figure 25 – Soil Sample 1 Experimental vs numerical nonlinear model comparison corresponding to the low-strain state

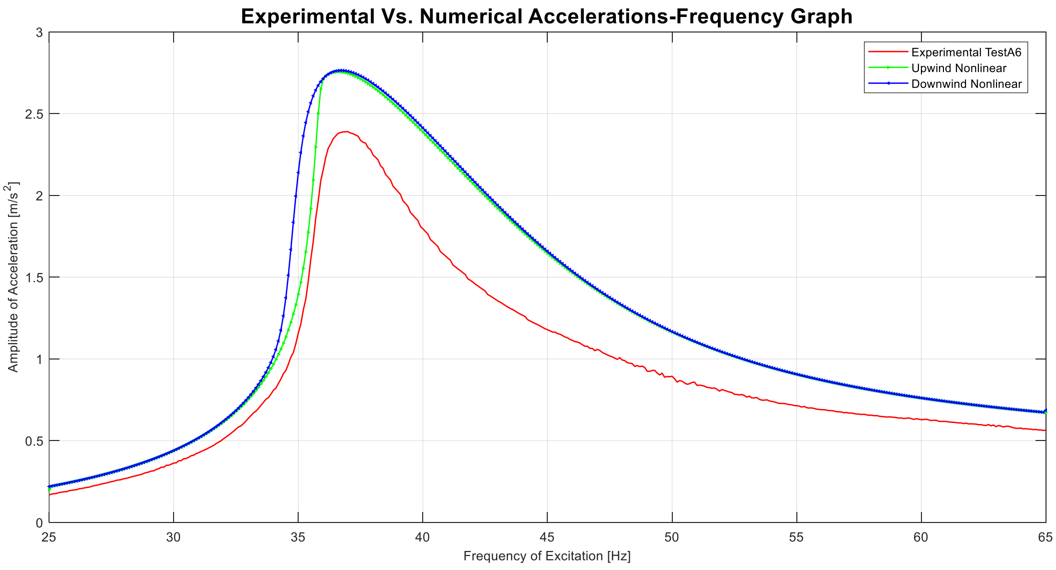

Figure 26 – Soil Sample 1 Medium-strain experimental vs numerical linear and nonlinear models comparison

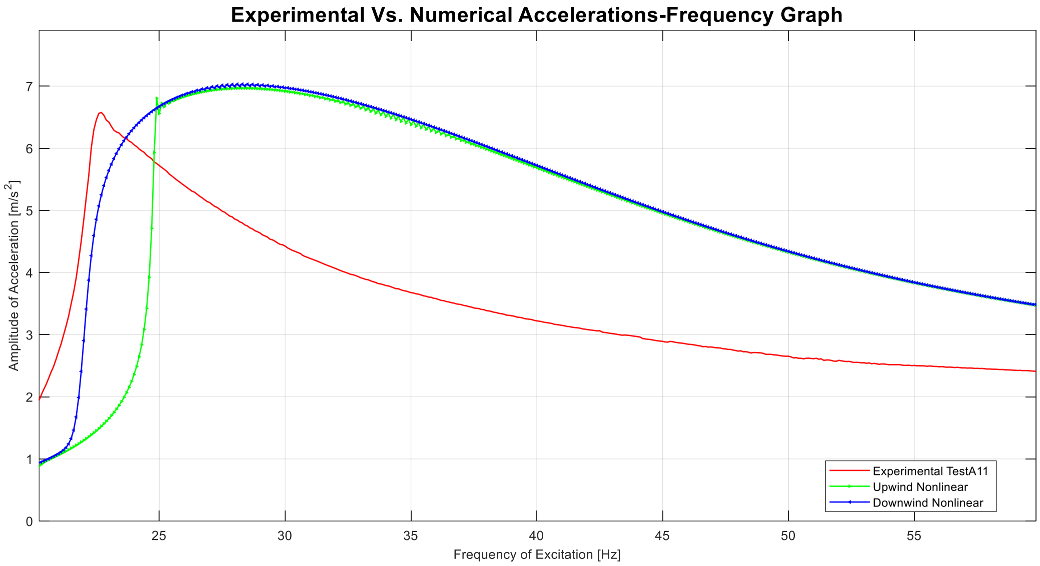

Figure 27 – Soil Sample 1 High-strain experimental vs numerical linear and nonlinear models comparison

5.3.1 Nonlinear model damping correction

While the hyperbolic soil model does capture the underlying characteristics of the nonlinear soil behaviour, as aforementioned, the simulated response still exhibits some discrepancies.

With the intent to correct the proposed model, some modifications will be implemented to it. Both the amplitude of the peaks and the shape of the curve, the two main differences between the experimental and the simulated response, are influenced by the damping term selected in the nonlinear model. As previously stated in Section 3.3, the damping term in the model is, for simplicity, chosen to be strain-independent. Theoretically, similarly to the shear modulus, the damping term should also be nonlinear.

Therefore, a second simulation analysis is repeated introducing a damping correction factor with the scope of eliminating these errors. The damping factor aims to multiply the linear model’s damping coefficient ζ, described in Section 4.1, such that the frequency-response curves match in correspondence to their maximum point. The damping correction factor (DCF) adopted for each test performed on Soil Sample 1 is reported in Table 5.

Test No.	DCF
1	1,45
2	1,50
3	1,35
4	1,30
5	1,25
6	1,20
7	1,20
8	1,20
9	1,20
10	1,20
11	1,20

Table 5 – Damping Correction Factor

The amplitude-frequency graphs of the simulated solution using the DCF implementation are presented in Figure 28 to Figure 30. With the applied modification, the low-strain test demonstrates a high degree of accuracy, while the medium-strain case, although not perfectly aligned with the experimental data, exhibits noticeable improvement. However, for the high-strain simulation, the modification does not yield similar enhancements. In this case, the adjustments fail to improve the accuracy of the solution.

Although the linear multiplication of the existing damping term led to a better match of the curves' amplitudes, the error in the shape of the curves grew as strain levels increased. This suggests that the damping nonlinearities in the model were incorrectly represented and that a simple correction factor doesn't bring a noticeable improvement. Specifically, the resonance shift was overestimated in low-strain tests and underestimated in high-strain tests. This discrepancy is less apparent in low-strain tests because the contribution of nonlinearities is smaller, making the errors less visually noticeable.

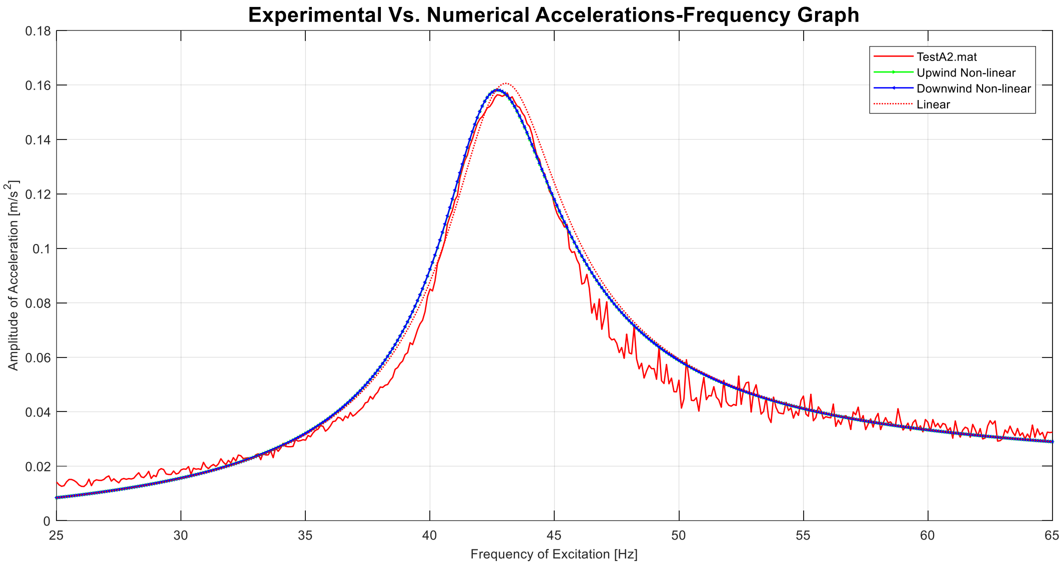

Figure 28 – Soil Sample 1 Low-strain experimental vs numerical linear and nonlinear models comparison with corrective damping

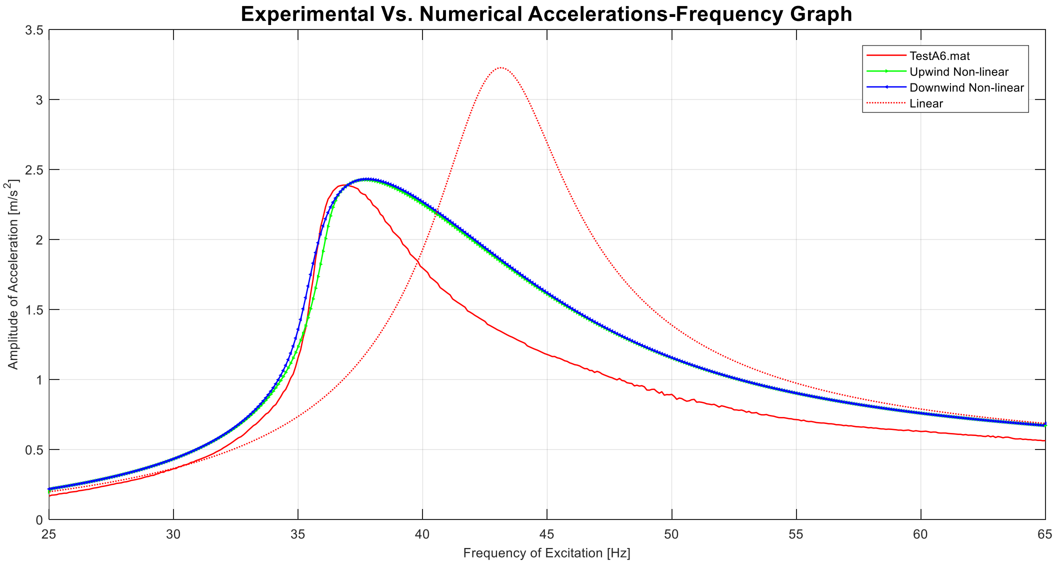

Figure 29 – Soil Sample 1 Medium-strain experimental vs numerical linear and nonlinear models comparison with corrective damping

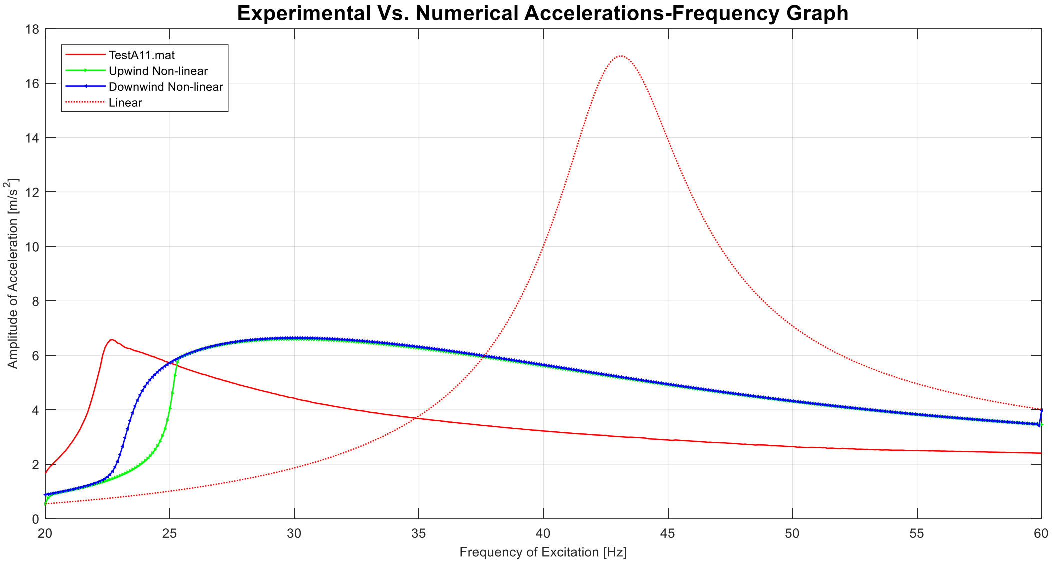

Figure 30 – Soil Sample 1 High-strain experimental vs numerical linear and nonlinear models comparison with corrective damping

An additional tool for evaluating the results is through the parameters γ_{error} and G_{error}, as described in Section 4.5. With the current DCF modification, these parameters show significant deviations, with errors (shown in Table 6) reaching up to 30%.

Test No.	γ_{error}	G_{error}
1	-18,1%	<1%
2	-14,5%	<1%
3	-14,7%	<1%
4	-15,4%	<1%
5	-12,4%	<1%
6	-13,8%	3,3%
7	-16,9%	6,4%
8	-19,4%	10,1%
9	-22,6%	14,1%
10	-24,6%	19,6%
11	-29,6%	26,6%

Table 6 – Values of γ_{error} and G_{error} for results using the nonlinear model with DCF implementation

In conclusion, the correction of the damping term using the DCF implementation demonstrates that the discrepancies between the simulated and the experimental solutions can be only partially improved. The simple multiplication of the linear damping coefficient may not be sufficient to correct both the amplitude and shape of the graph.

5.3.2 Nonlinear model radius correction

Having just concluded that a simple multiplication of the damping term doesn’t bring significant improvements to the results, a second corrective approach was introduced. This correction involves adjusting the radius at which we consider the representative strain state for the whole specimen cross-section. In other words, the strain is directly proportional to the radius (see Eq.2) and one must select only one radius value at which the strain state is representative of the whole cross-section. The larger the r_{obs}, the larger the nonlinearity. Although r_{obs} should remain constant throughout the tests, previously set to 0.6 times the soil sample radius (in Section 3.1), it is modified here to demonstrate the influence of this parameter on the obtained results.

Both the DCF and r_{obs} are adjusted to ensure that the γ_{error} and G_{error} parameters, described in Section 4.5, do not exceed 1% and the numerical solution’s peak aligns with the experimental curve. The adopted r_{obs} and DCF values for each test on Soil Sample 1 are presented in Table 7.

Test No.	DCF	r_{obs}
1	0,49	0,25
2	0,64	0,30
3	0,71	0,37
4	0,82	0,45
5	0,91	0,50
6	1,00	0,58
7	1,06	0,64
8	1,09	0,68
9	1,09	0,70
10	1,11	0,74
11	1,13	0,80

Table 7 – Damping Correction Factor and r_{obs}

The amplitude-frequency graphs of the solution with the DCF and the r_{obs} implementation are shown in Figure 31 to Figure 33.

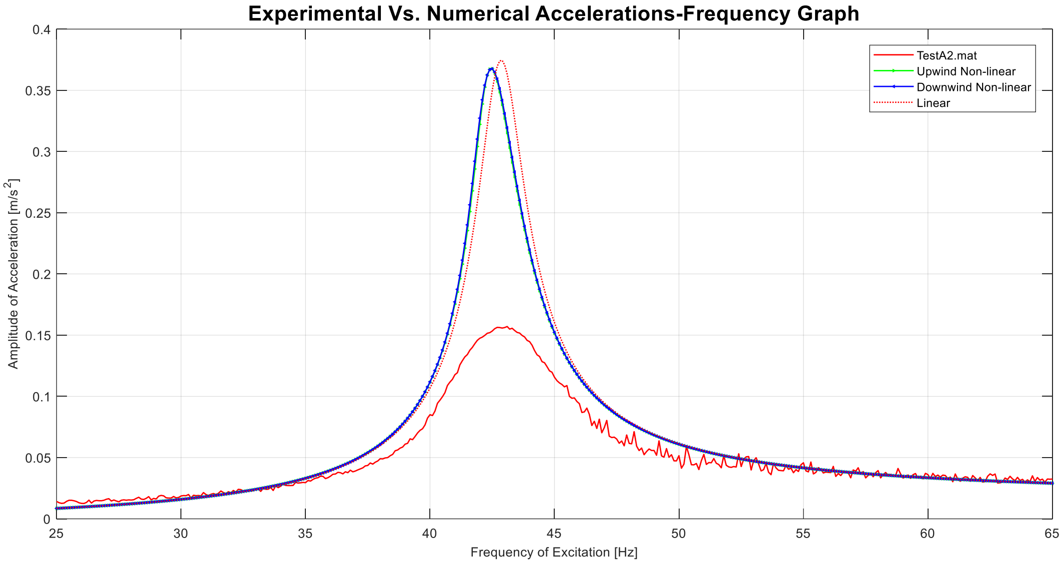

Figure 31 – Soil Sample 1 Low-strain experimental vs numerical linear and nonlinear models comparison with corrective radius and damping

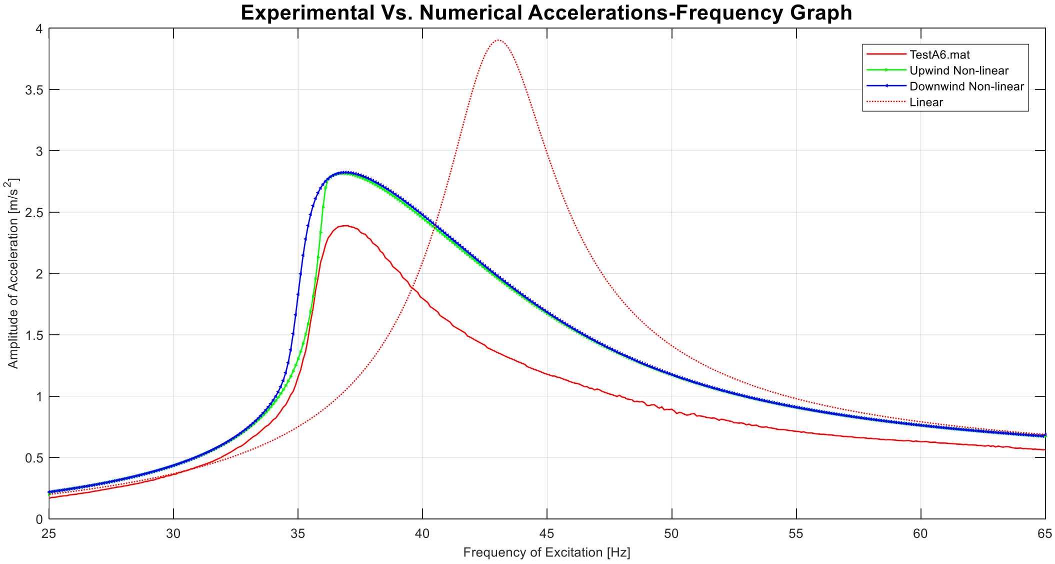

Figure 32 – Soil Sample 1 Low-strain experimental vs numerical linear and nonlinear models comparison with corrective radius and damping

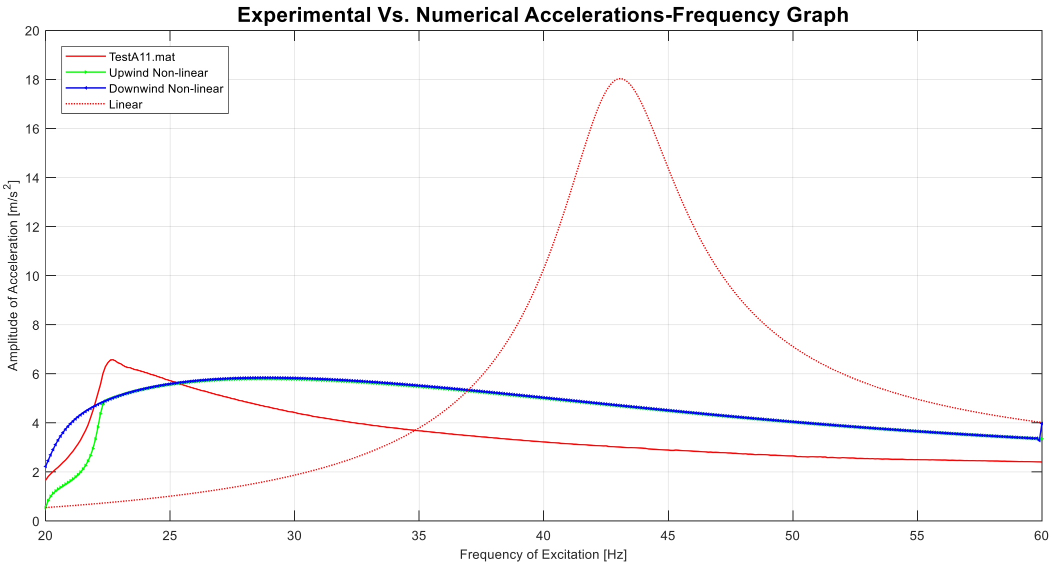

Figure 33 – Soil Sample 1 High-strain experimental vs numerical linear and nonlinear models comparison with corrective radius and damping

The analysis of these three plots provides a key insight into improving the nonlinear model. Although the model’s solutions remain far from perfectly matching the experimental results, it becomes evident that the primary issue likely lies in the damping term. A simple linear modification of the current set-up was insufficient to obtain the sought-after results. Unlike the shear modulus, the current damping term should most likely be modelled as strain-dependent, and not assumed constant as done in the current study. To achieve closer agreement with the experimental results, particularly near the peak, a strain-dependent damping term must be introduced.

Chapter 6 – Conclusions

This study aimed to evaluate the performance of a nonlinear numerical model in capturing soil behaviour under dynamic loading conditions. Through a systematic analysis of super-harmonics, comparisons between linear and nonlinear models, and the validation of the nonlinear model against experimental results, key insights were obtained regarding the model's accuracy and limitations.

Firstly, the contribution of super-harmonics to the numerical solution was assessed. The results demonstrated that for low- and medium-strain states, the third and fifth harmonics were orders of magnitude smaller than the first harmonic, making their contribution negligible. Even in high-strain tests, where nonlinear effects became more pronounced, the impact of higher-order harmonics remained limited. Consequently, it was concluded that super-harmonics can be disregarded in future comparative analyses between the numerical and experimental responses, simplifying the model implementation.

Secondly, the comparison between linear and nonlinear models highlighted the significance of incorporating nonlinear material behaviour, without increasing the execution time significantly. The simulations took a maximum of 5 minutes each to be executed on a portable computer with 16GB RAM, and therefore are easily made faster if executed on a more powerful device. At low strain levels, the nonlinear model closely resembled the linear solution, as expected due to minimal nonlinearity. However, as the strain increased, the nonlinear model successfully captured the resonance shift observed in experimental data, while the linear model failed to do so. This confirmed that the nonlinear model more accurately represents the soil response by accounting for apparent softening effects.

Furthermore, the comparison between the nonlinear model's response and experimental results demonstrated a strong correlation across most strain states. The model accurately replicated the shift in resonance frequency and the general shape of the response curve at low and medium strain levels. However, discrepancies emerged at higher strain levels, where the model overestimated acceleration amplitudes near resonance and produced a more damped response than observed experimentally. This indicated a misrepresentation of damping within the model.

To address this issue, two corrective approaches were explored: the implementation of a damping correction factor (DCF) and an adjustment to the representative strain radius (r_{obs}). The DCF improved the amplitude-frequency response at low and medium strain levels but failed to resolve discrepancies at high strain states. Additionally, the implementation of an adjusted r_{obs} value yielded better results by reducing the overall error. However, neither correction was sufficient to achieve a perfect match with experimental data.

The primary limitation identified in the model is the assumption of a strain-independent damping term. The results suggest that, like the shear modulus, damping should be modelled as a strain-dependent parameter. Implementing a more advanced damping formulation that evolves with strain could enhance the model's accuracy, particularly at high-strain levels where current discrepancies remain significant.

In conclusion, this study confirmed the effectiveness of the nonlinear numerical model in capturing the essential characteristics of soil behaviour under dynamic loading. While the model accurately reproduces key nonlinear effects, further refinement, particularly in the damping representation, is necessary to improve its agreement with experimental data. Future research should focus on developing a strain-dependent damping function to enhance model accuracy and ensure more precise predictive capabilities for high-strain dynamic soil behaviour.

Chapter 7 – Recommendations and Discussions

In this section, further discussions regarding the abovementioned results are presented. It also gives meaningful leads on how to continue with this research, and which aspects of it could be improved.

7.1 Numerical solver issues

The nonlinear model was solved with the aid of the numerical solver BVP4C. Despite this solver being especially useful in modelling the dynamic boundary conditions, it also revealed some issues.

A problem emerged when solving for high-strain tests, where the solver identified incorrect solutions satisfying the equations of motion. These inaccuracies appeared in the post-resonance region of the upwind solution, highlighted by the orange circle in Figure 34. At these frequencies, the solver exhibited an initial error, which progressively increased with subsequent frequencies due to divergence, and subsequently influenced the downwind solution too.

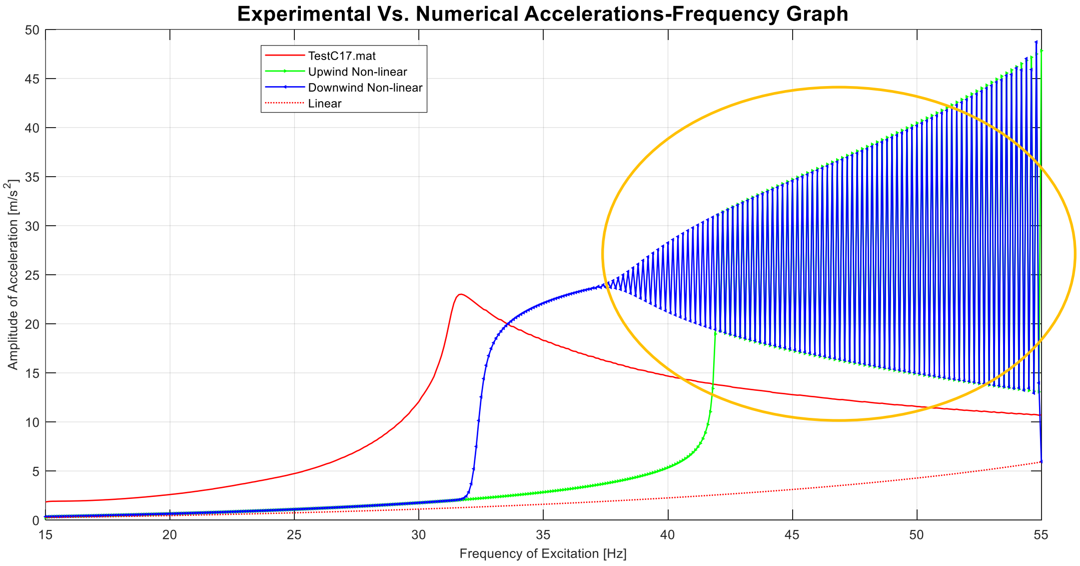

Figure 34 – BVP4C solver numerical error

The BVP4C solver has a built-in function that allows the user to determine the solution's required accuracy. However, this was not sufficient to eliminate the numerical error, leading to the search for other methods to solve the problem.

The equation of motion could also be solved using numerical methods such as the Finite Element Method (FEM), which is well-suited for solving partial differential equations in two or three spatial dimensions.

7.2 Bottom boundary condition implementation

The linear and nonlinear models used in this project to analyse the response of the soil to the dynamic loading adopted a theoretical approach when describing the boundary conditions. This approach was limited in mathematically depicting the functioning of the RCT apparatus; a fixed base and free top with the inertial contribution of the active plate. However, an important assumption was made in this method, hypothesising that the contacts between the soil sample and the top and bottom plates were perfectly fixed. In reality, at high strain levels, the accelerations may be significant to the point that a slight slip may occur on the contact surface.

To address this issue, a potential solution is to incorporate a high-stiffness rotational spring to model the interfaces more accurately. A more refined approach could involve modifying the spring stiffness from linear to bilinear, accounting for slip only beyond a specific strain threshold. This configuration is schematised in Figure 35.

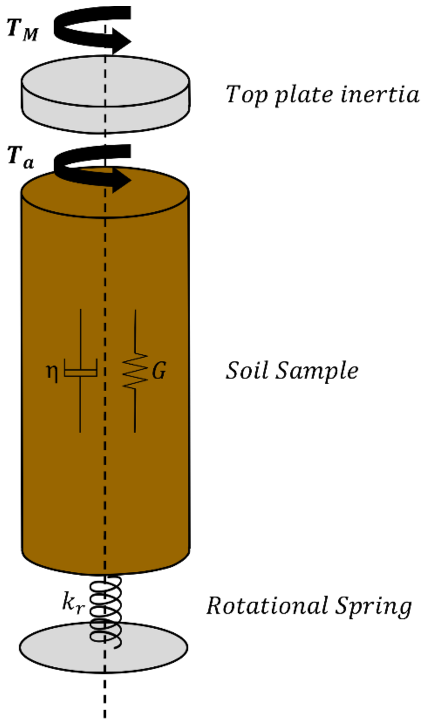

Figure 35 - Modified boundary conditions' configuration

This new configuration will shift the peak of the amplitude-frequency graph to the left, simulating a slight change in the natural frequency of the soil sample.

7.3 Soil granulometry dependence

The different soil samples tested in this research were all sandy lean clays, with similar granulometry. This influenced the responses of the soil samples, which consequently, behaved similarly under the same forcing. For a more extensive analysis, the model could be tested using clean sands in the future.

Under cyclic forcing, saturated non-cohesive and cohesive soils exhibit distinct responses due to differences in their structure, permeability, and drainage characteristics.

In saturated non-cohesive soils, such as sands, cyclic loading can lead to progressive densification or liquefaction, depending on the soil's density and drainage conditions. Pore water pressure tends to increase with repeated loading, reducing effective stress and potentially leading to a loss of shear strength.

The permeability of non-cohesive soils allows for relatively high water velocity within the pore spaces, facilitating drainage and dissipation of excess pore pressures if the loading frequency permits. In contrast, saturated cohesive soils, like clays, have low permeability, causing a much slower response to cyclic loading. The restricted water movement within the fine-grained matrix results in a buildup of excess pore pressure with limited immediate drainage, potentially leading to cyclic softening or progressive accumulation of strain over time.

References

[1] E. Commission, "The European Green Deal," 2020. [Online]. Available: https://commission.europa.eu/.

[2] "Offshore Wind in Europe - Key trends and statistics," Wind Europe, 2019. [Online]. Available: http://www.ewea.org.

[3] M. M. Futai, J. Dong, S. K. Haigh and S. G. Madabhushi, "Dynamic response of monopiles in sand using centrifuge modelling," *Soil Dynamics and Earthquake Engineering,* vol. 115, pp. 90-103, 2018.

[4] F. Stockhert, Fracture Mechanics applied to Hydraulic Fracturing in Laboratory Experiments, Bochum, 2015.

[5] D. M. Wood, "Soil behaviour and critical state soil mechanics," 1990.

[6] i. Vardoulakis, "Stress-strain models for granular materials and their applications to landslides," 1984.

[7] J. M. Duncan and C. Y. Chang, "Nonlinear analysis of stress and strain in soils," *Journal of the Soil Mechanics and Foundations Division,* vol. 95, pp. 1629-1653, 1970.

[8] A. G. Shirzoi, B. Zhang, B. Han and S. Dai, "Influence of soil hysteretic damping on lateral response of offshore wind turbine monopile in sandy soil," *Marine Georesources & Geotechnology,* 2025.

[9] J. Zhou, L. Zhang, W. Peng and Z. Xu, "Numerical study on soil-arching behavior in pile-supported embankments with pile settlement by developed damping spring-based trapdoor model," *International Journal for Numerical and Analytical Methods in Geomechanics.,* 2025.

[10] Y. Zhang, K. K. Aamodt and A. M. Kaynia, "Hysteretic damping model for laterally loaded piles," *Marine Structures,* vol. 76, 2021.

[11] L. Wang, S. Wang and Y. Hong, "A dynamic py+ M-θ model for monopile in soft clay considering failure mechanism under combined actions of wind and earthquake," *Computers and Geotechnics,* 2025.

[12] G. Gatti and B. Cochelin, "On the use of higher order harmonics in the harmonic balance method," *Journal of Sound and Vibration,* 2020.

[13] T. Detroux, L. Renson, G. Kershen and J. C. Golinval, "The harmonic balance method for bifurcation analysis of large-scale nonlinear mechanical systems," *Computer Methods in Applied Mechanics and Engineering,* vol. 296, pp. 18-38, 2015.

[14] K. Yamamoto, G. Kerschen and K. Shirasaka, "A generalized harmonic balance method for analyzing nonlinear mechanical systems with strong nonlinearities.," *Nonlinear Dynamics,* vol. 91, pp. 853-869.

[15] D. Lo Presti, M. Jamiolkowski, O. Pallara, A. Cavallaro and S. Pedroni, " Shear modulus and damping of soils," *Géotechnique,* 1997.

[16] I. A. van der Esch, A. B. Faragau, K. van Dalen, A. Metrikine and F. Pisanò, "Modelling the steady-state motion of a soil column including nonlinear hysteretic damping under periodic excitations," 2020.

[17] D. C. F. Lo Presti, O. Pallara, R. Lancellotta, M. Armandi and R. Maniscalo, "Monotonic and Cyclic Loading Behavior of Two Sands at Small Strains," *Geotechnical Testing Journal,* vol. 16, pp. 409-424, 1993.

[18] R. Davoodi-Bilesavar and L. R. Hoyos, "Response of cohesive–frictional soils at small to medium shear strain levels from thermo-controlled resonant column testing," *Canadian Geotechnincal Journal,* vol. 61, 2023.

[19] V. P. Drnevich, S. Werden, J. C. Ashlock and J. R. Hall Jr., "Applications of the New Approach to Resonant Column Testing," *Geotechnical Testing Journal,* vol. 38, pp. 23-39, January 2015.

[20] A. T. F. Chen and K. H. Stokoe, "Interpretation of Strain-Dependent Modulus and Damping From Torsional Soil Tests," p. 44, 1979.

[21] S. K. Werden, V. P. Drnevich and J. R. Hall, "New Approach to Resonant Column Testing," *Geotechnical Testing Journal,* vol. 36, 2013.

[22] B. O. Hardin and V. P. Drnevich, "Shear Modulus and Damping in Soils: Measurement and Parameter Effects," *Journal of the Soil Mechanics and Foundations Division,* vol. 98, 1972.

[23] A. Ciancimino, R. M. Cosentini, S. Fot, G. Lanzo, A. Pagliaroli and O. Pallara, "The PoliTO–UniRoma1 database of cyclic and dynamic laboratory tests: assessment of empirical predictive models," *Bulletin of Earthquake Engineering,* p. 2569–2601, 2023.

[24] V. S. Huigen, K. van Dalen, A. Metrikine, A. Faragau and S. Panagoulias, "Monopile foundation modeling in the frequency domain for Offshore Wind Turbines," 2021.

[25] P. Saloni and S. Ajanta, "Effect of frequency and amplitude on dynamic behaviour, stiffness degradation and energy dissipation of saturated cohesive soil," *Geomechanics and Geoengineering,* vol. 17, pp. 30-44, 2019.

[26] V. P. Drnevich and J. C. Ashlock, "Measurement of Damping in Soils by the Resonant Column Test," 2017.

Annex A

All frequency-acceleration graphs of Soil Sample 2 and Soil Sample 3 are shown in Annex A.

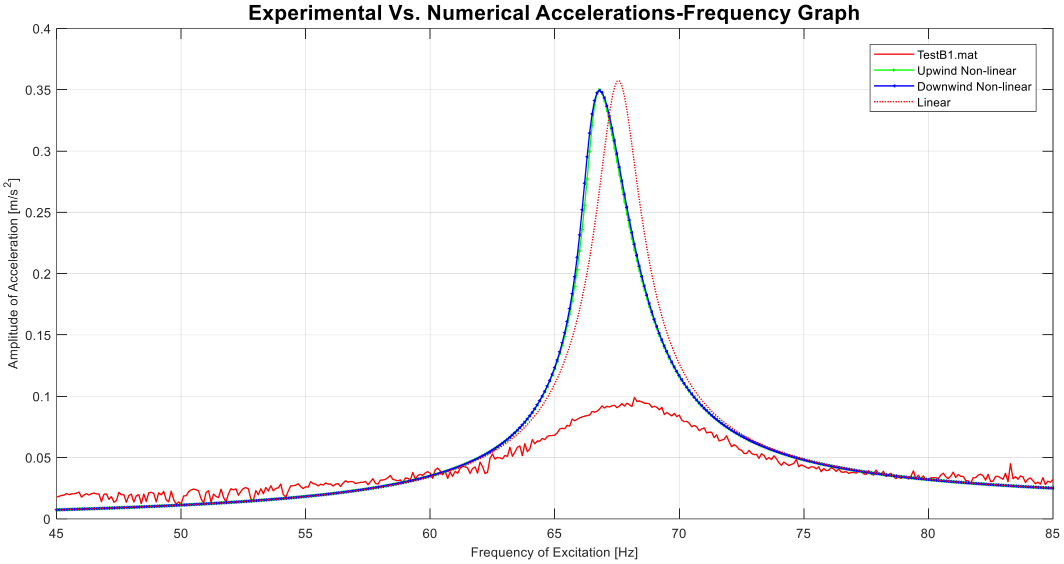

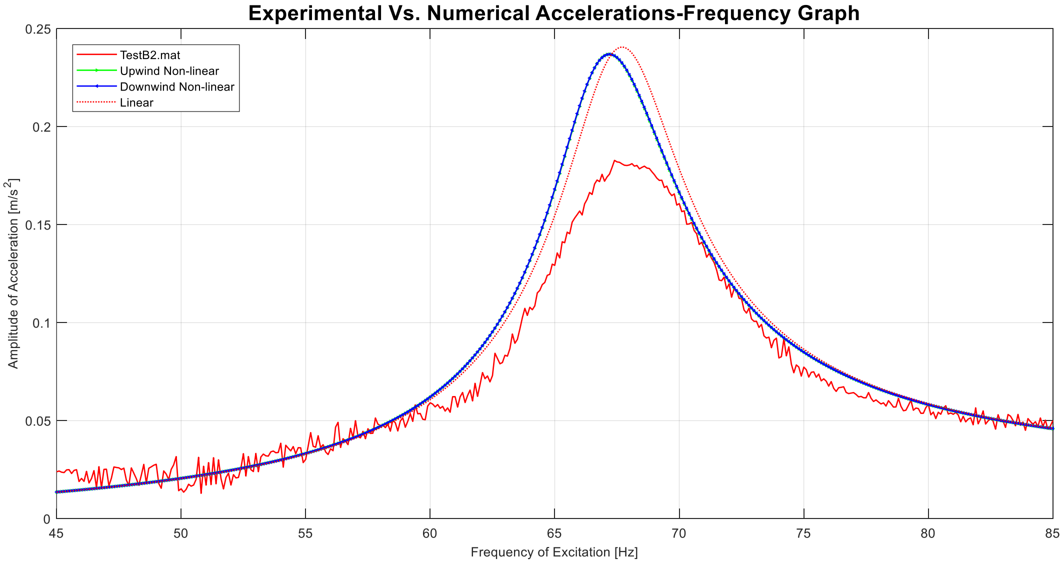

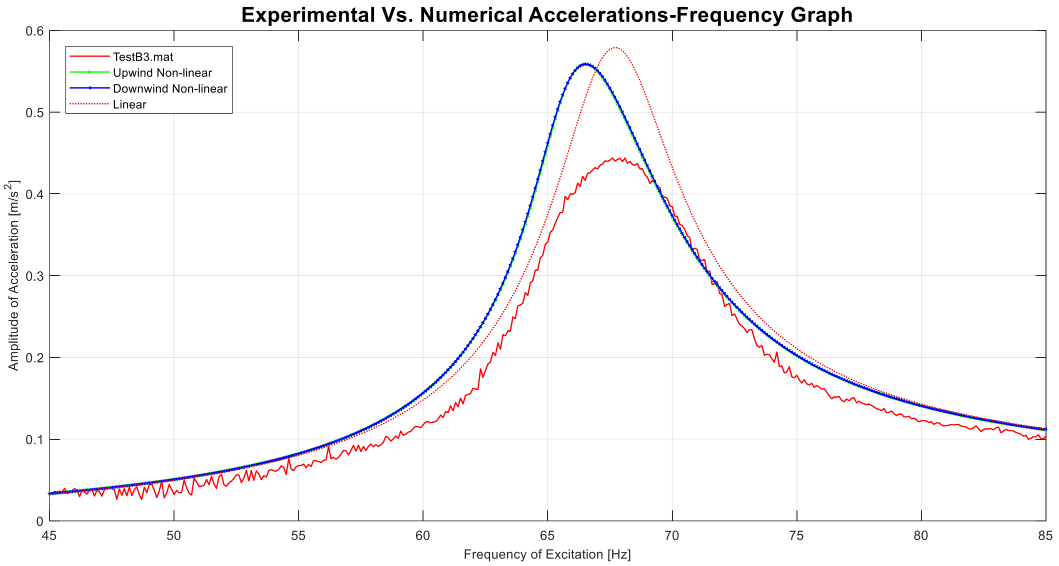
Experimental Vs. Numerical Accelerations-Frequency Graph
TestB3.mat
Upwind Non-linear
Downwind Non-linear
Linear
Amplitude of Acceleration [m/s^2]
0
0.1
0.2
0.3
0.4
0.5
0.6
45
50
55
60
65
70
75
80
85
Frequency of Excitation [Hz]

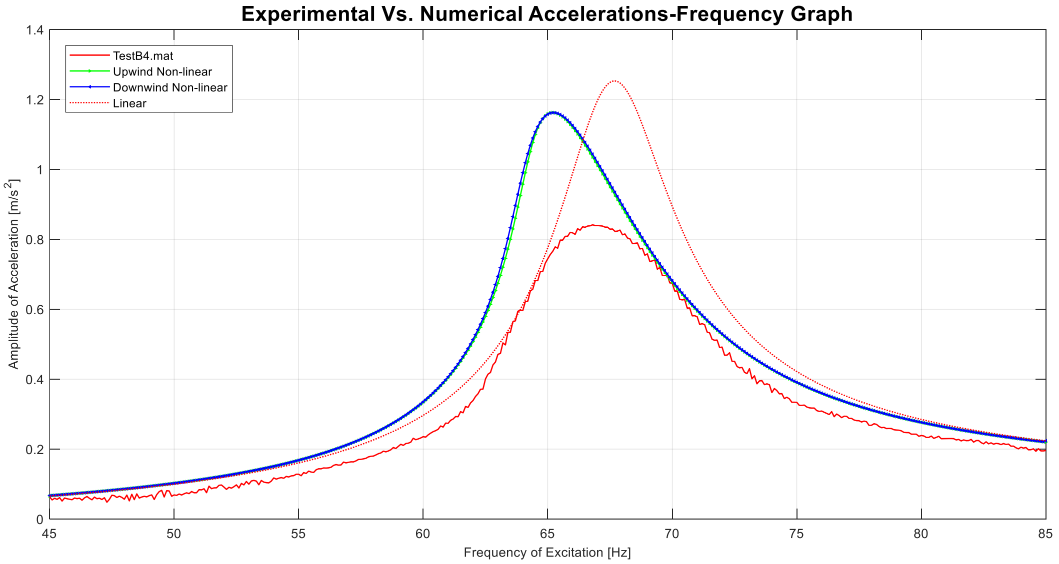
Experimental Vs. Numerical Accelerations-Frequency Graph
TestB4.mat
Upwind Non-linear
Downwind Non-linear
Linear
Amplitude of Acceleration [m/s^2]
0
0.2
0.4
0.6
0.8
1
1.2
1.4
45
50
55
60
65
70
75
80
85
Frequency of Excitation [Hz]

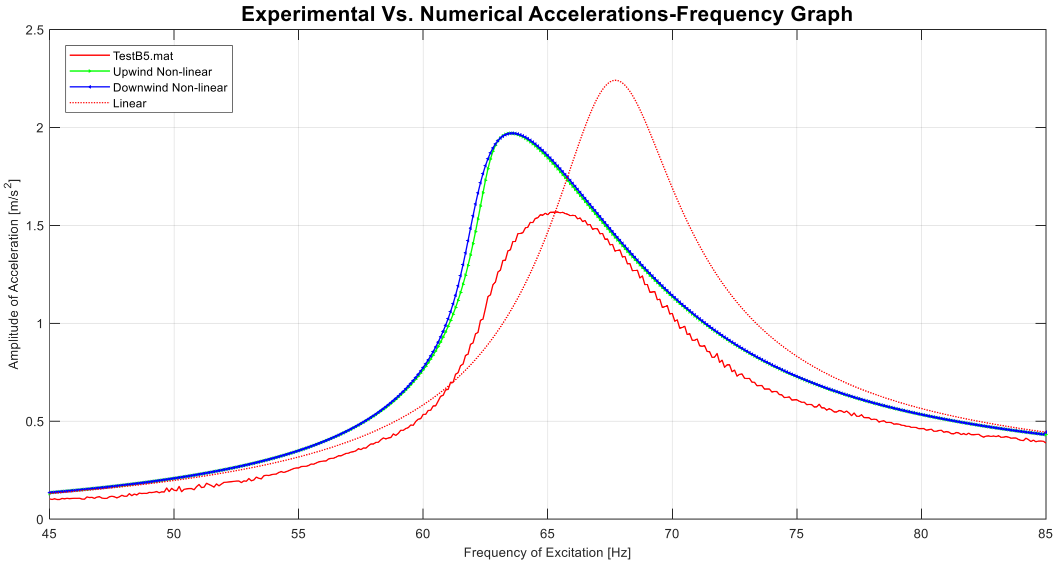
Experimental Vs. Numerical Accelerations-Frequency Graph
TestB5.mat
Upwind Non-linear
Downwind Non-linear
Linear
Amplitude of Acceleration [m/s^2]
0
0.5
1
1.5
2
2.5
45
50
55
60
65
70
75
80
85
Frequency of Excitation [Hz]

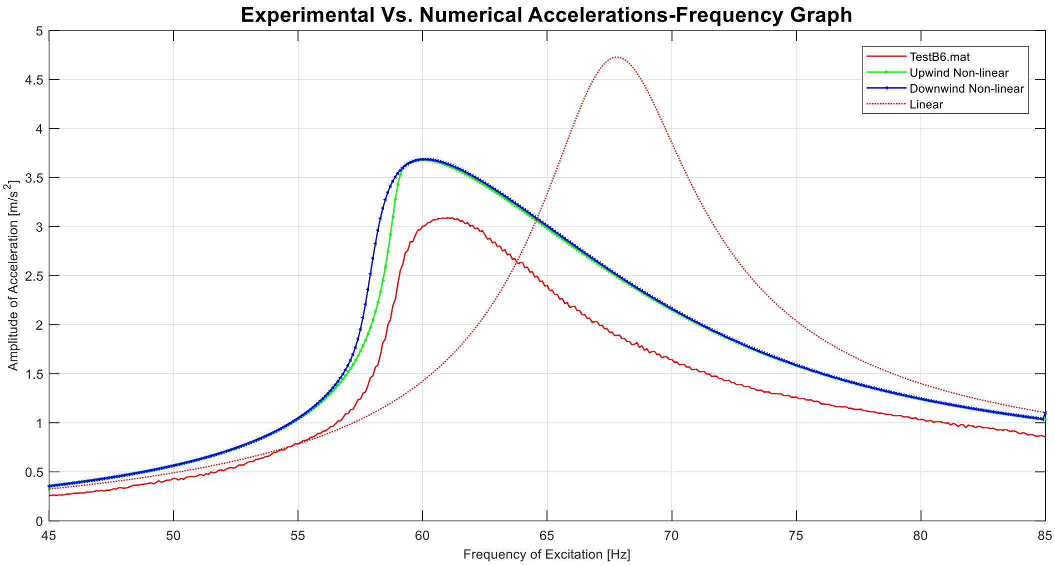
Experimental Vs. Numerical Accelerations-Frequency Graph

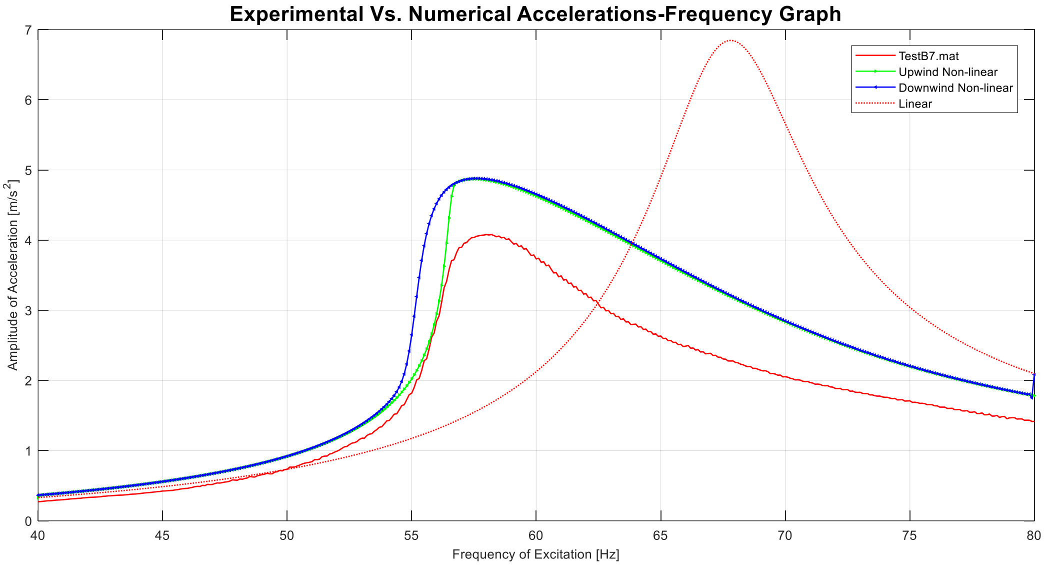
Experimental Vs. Numerical Accelerations-Frequency Graph

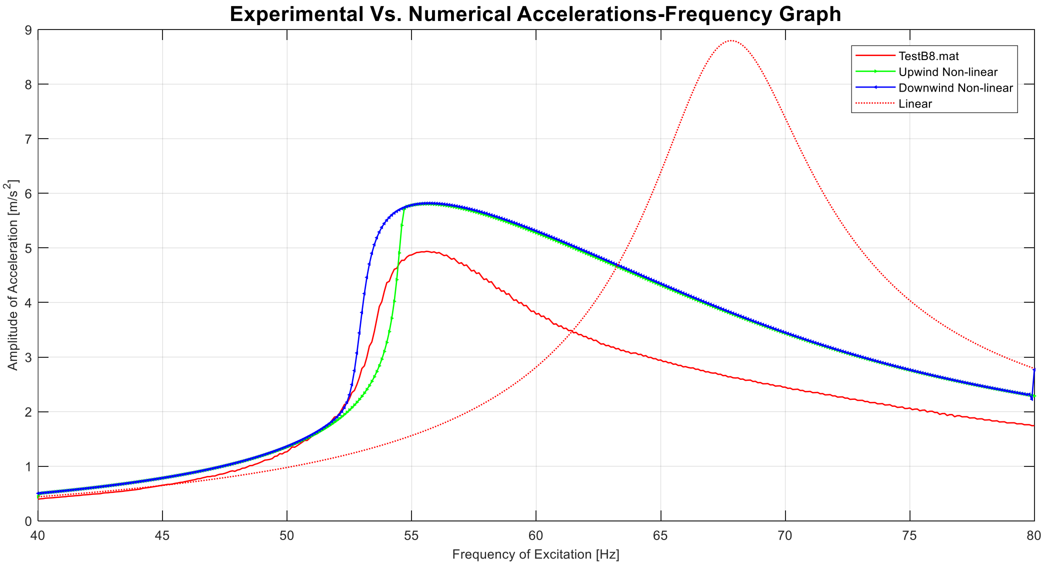
Experimental Vs. Numerical Accelerations-Frequency Graph

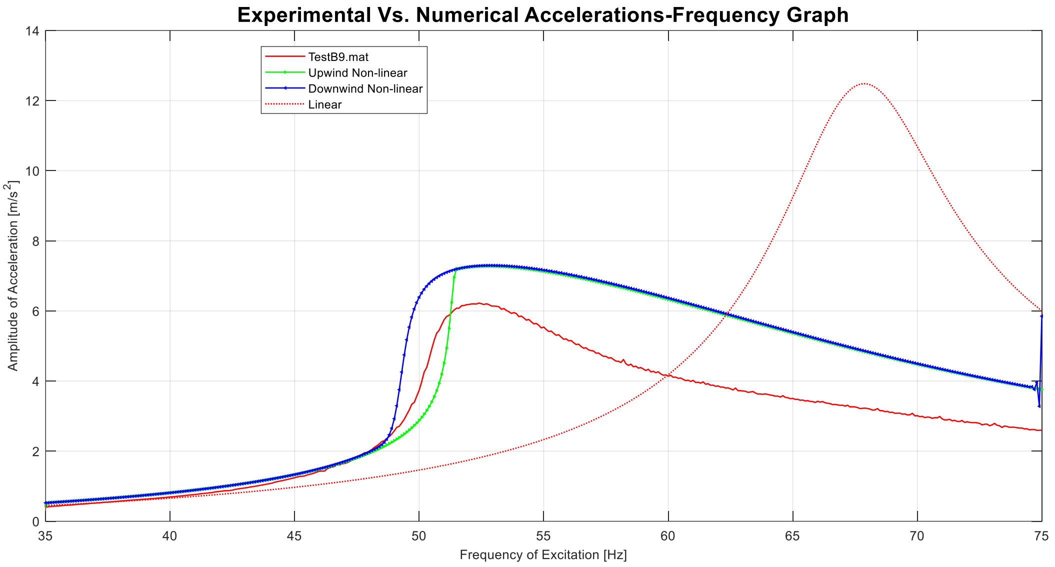
Experimental Vs. Numerical Accelerations-Frequency Graph
TestB9.mat
Upwind Non-linear
Downwind Non-linear
Linear
Amplitude of Acceleration [m/s^2]
0
2
4
6
8
10
12
14
35
40
45
50
55
60
65
70
75
Frequency of Excitation [Hz]

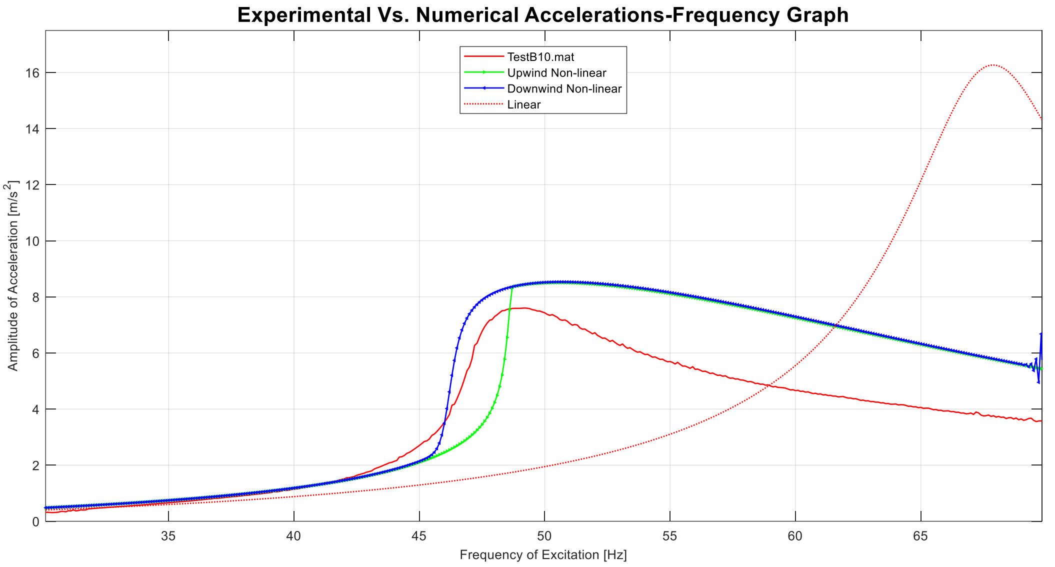
Experimental Vs. Numerical Accelerations-Frequency Graph
TestB10.mat
Upwind Non-linear
Downwind Non-linear
Linear
Amplitude of Acceleration [m/s^2]
0
2
4
6
8
10
12
14
16
35
40
45
50
55
60
65
Frequency of Excitation [Hz]

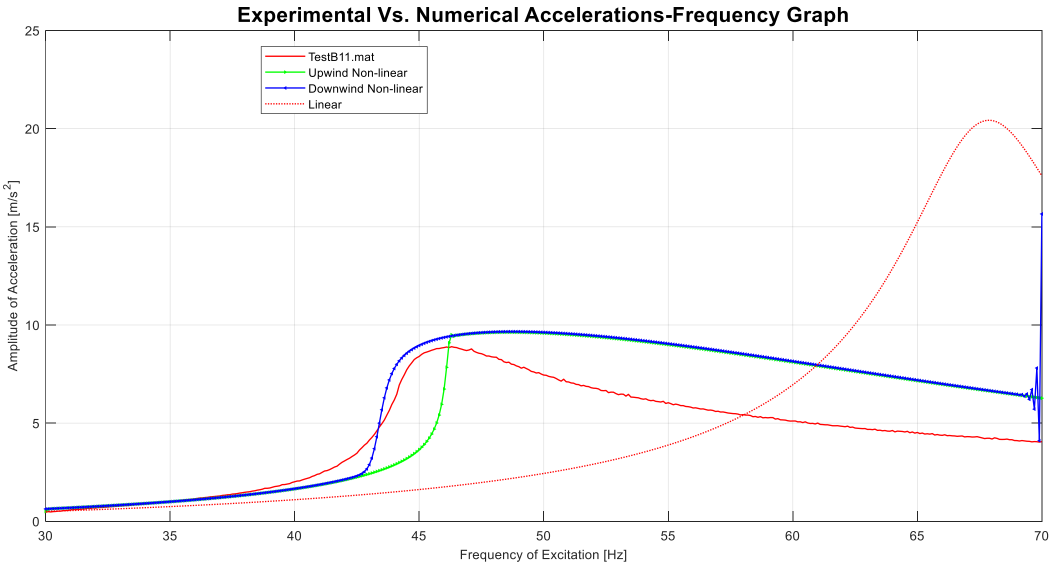
Experimental Vs. Numerical Accelerations-Frequency Graph
TestB11.mat
Upwind Non-linear
Downwind Non-linear
Linear
Amplitude of Acceleration [m/s^2]
0
5
10
15
20
25
30
35
40
45
50
55
60
65
70
Frequency of Excitation [Hz]

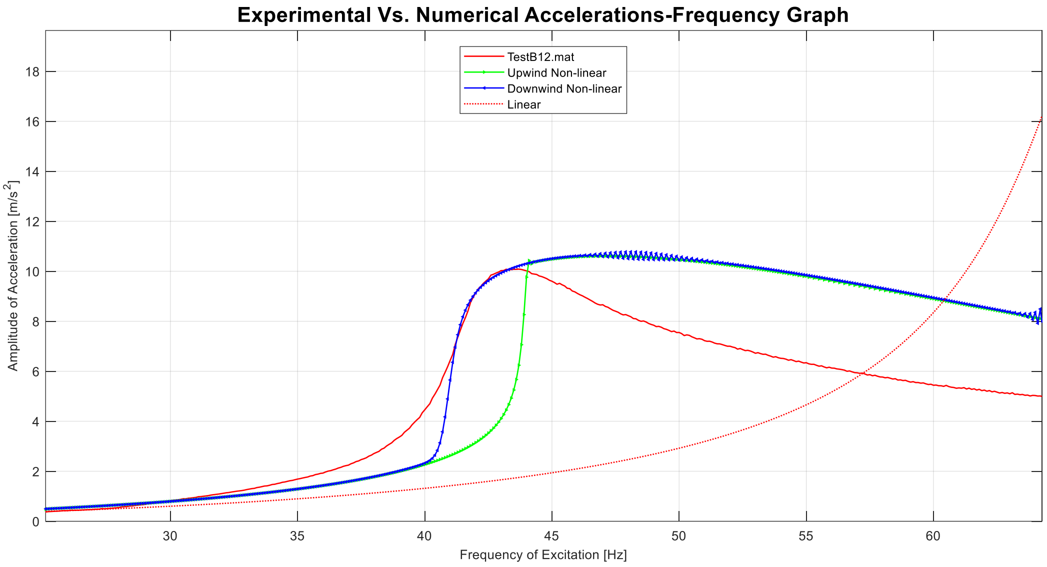
Experimental Vs. Numerical Accelerations-Frequency Graph
TestB12.mat
Upwind Non-linear
Downwind Non-linear
Linear
Amplitude of Acceleration [m/s^2]
Frequency of Excitation [Hz]
0
2
4
6
8
10
12
14
16
18
30
35
40
45
50
55
60

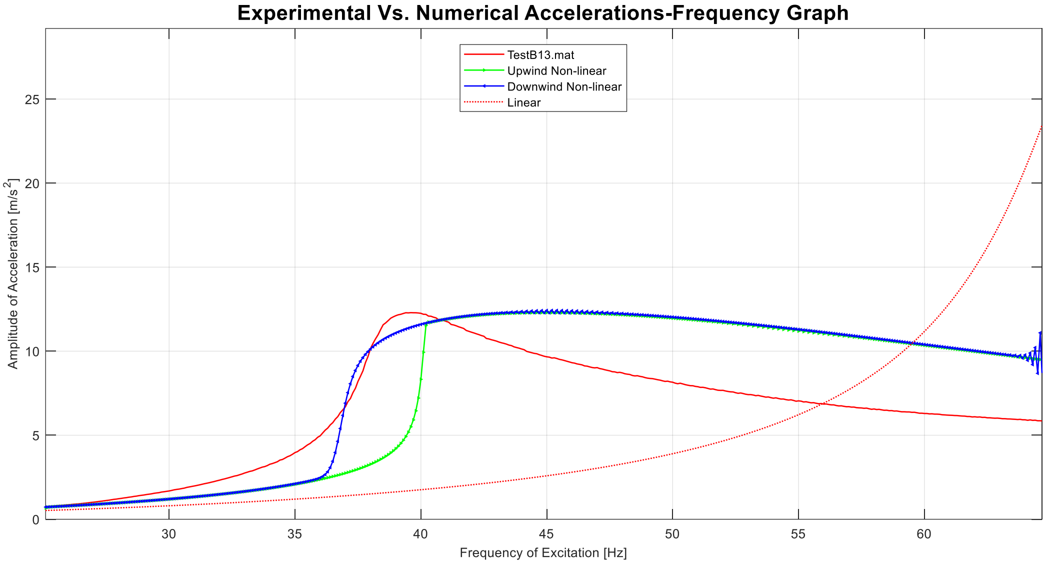
Experimental Vs. Numerical Accelerations-Frequency Graph
TestB13.mat
Upwind Non-linear
Downwind Non-linear
Linear
Amplitude of Acceleration [m/s^2]
Frequency of Excitation [Hz]
0
5
10
15
20
25
30
35
40
45
50
55
60

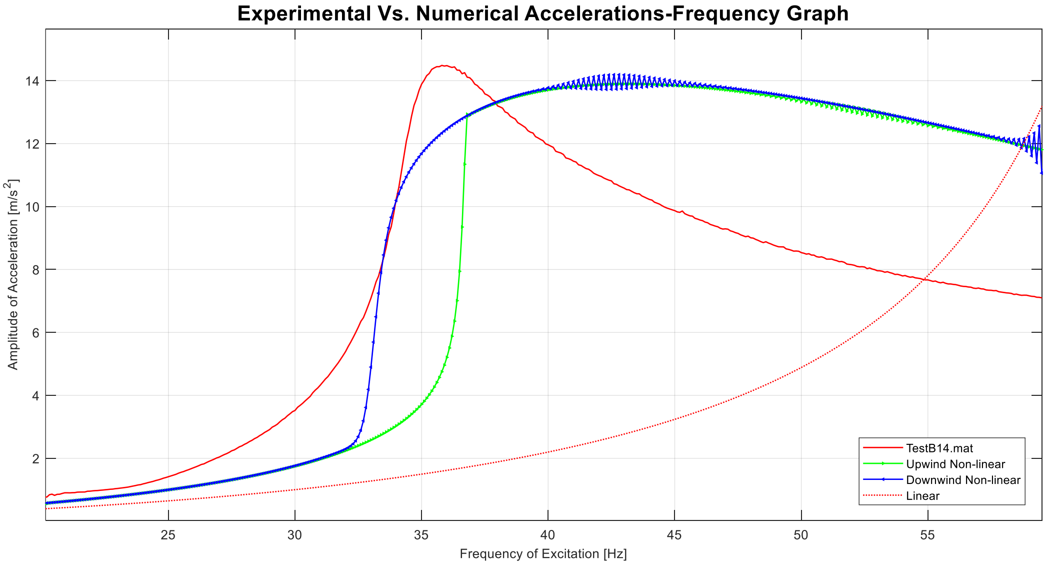
Experimental Vs. Numerical Accelerations-Frequency Graph
TestB14.mat
Upwind Non-linear
Downwind Non-linear
Linear
Amplitude of Acceleration [m/s^2]
Frequency of Excitation [Hz]
2
4
6
8
10
12
14
25
30
35
40
45
50
55

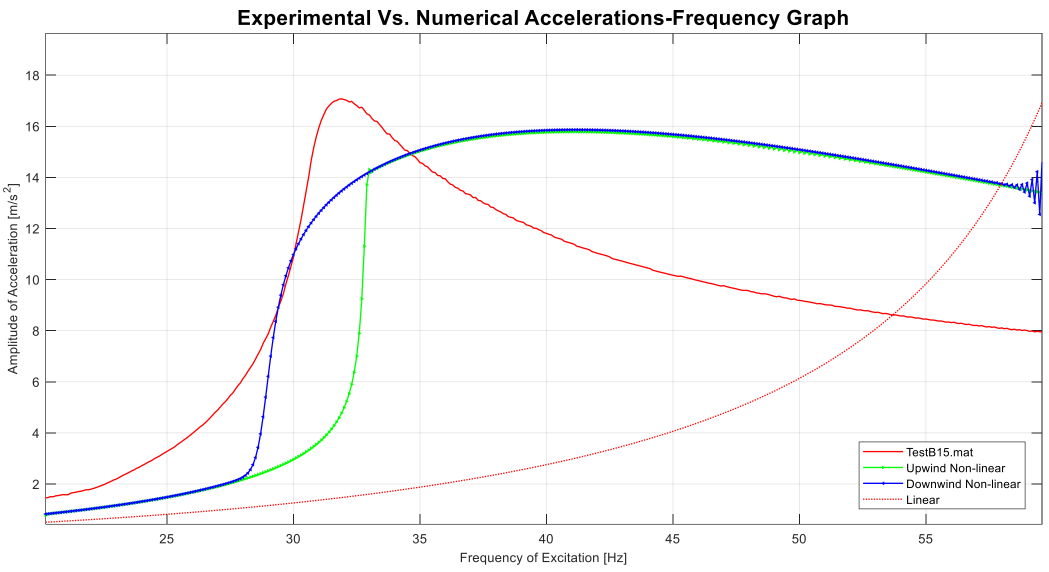
Experimental Vs. Numerical Accelerations-Frequency Graph
Amplitude of Acceleration [m/s^2]
18
16
14
12
10
8
6
4
2
25
30
35
40
45
50
55
Frequency of Excitation [Hz]
TestB15.mat
Upwind Non-linear
Downwind Non-linear
Linear

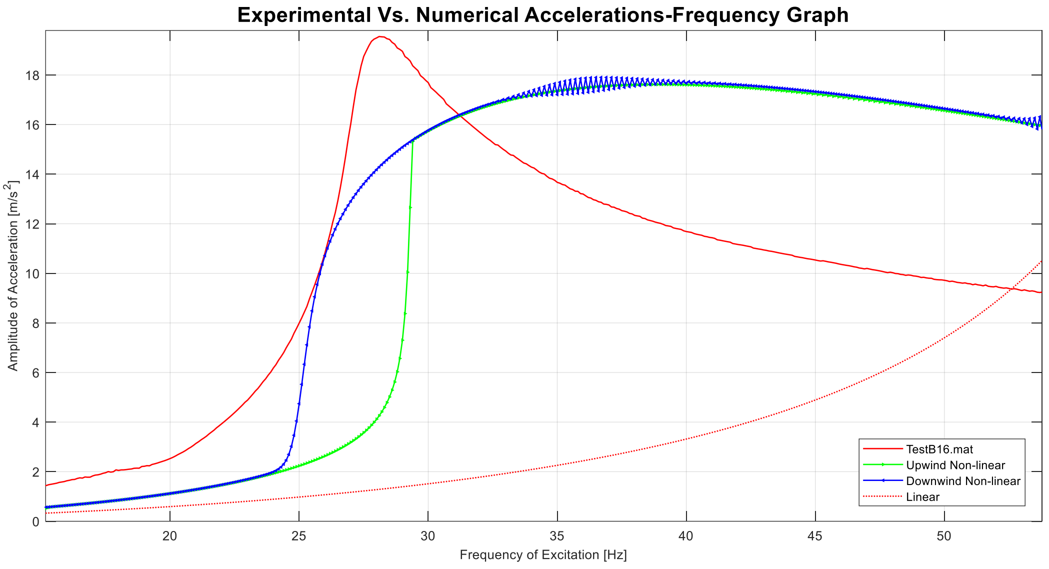
Experimental Vs. Numerical Accelerations-Frequency Graph
Amplitude of Acceleration [m/s^2]
18
16
14
12
10
8
6
4
2
0
20
25
30
35
40
45
50
Frequency of Excitation [Hz]
TestB16.mat
Upwind Non-linear
Downwind Non-linear
Linear

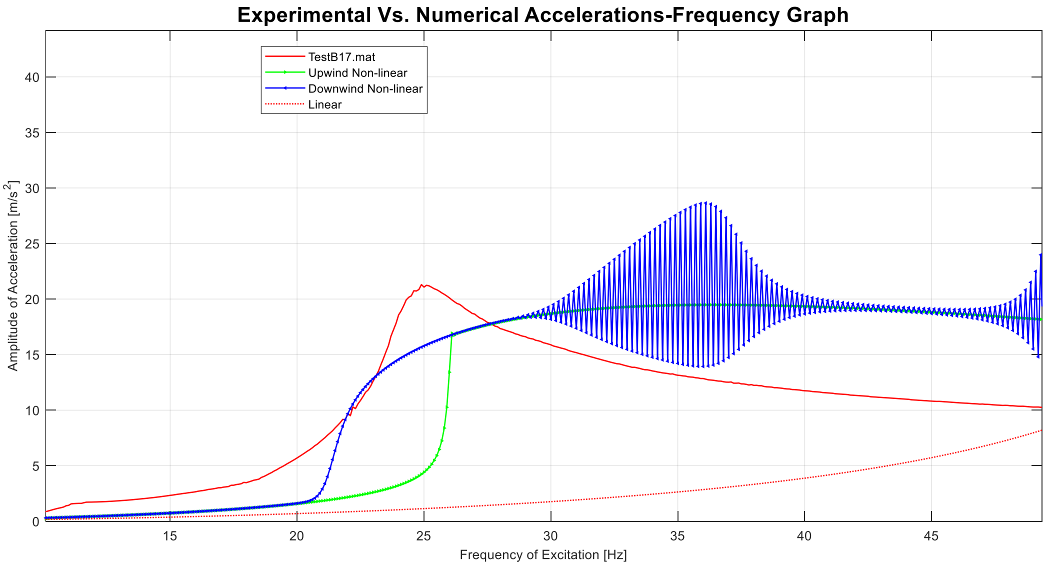
Experimental Vs. Numerical Accelerations-Frequency Graph
TestB17.mat
Upwind Non-linear
Downwind Non-linear
Linear
Amplitude of Acceleration [m/s^2]
40
35
30
25
20
15
10
5
0
15
20
25
30
35
40
45
Frequency of Excitation [Hz]

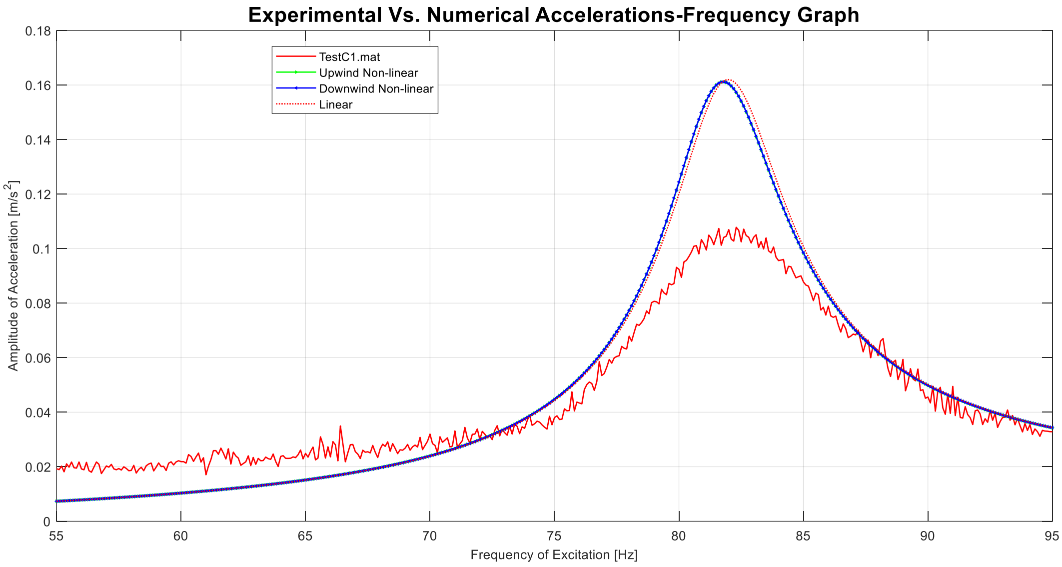
Experimental Vs. Numerical Accelerations-Frequency Graph
TestC1.mat
Upwind Non-linear
Downwind Non-linear
Linear
Amplitude of Acceleration [m/s^2]
0
0.02
0.04
0.06
0.08
0.1
0.12
0.14
0.16
0.18
55
60
65
70
75
80
85
90
95
Frequency of Excitation [Hz]

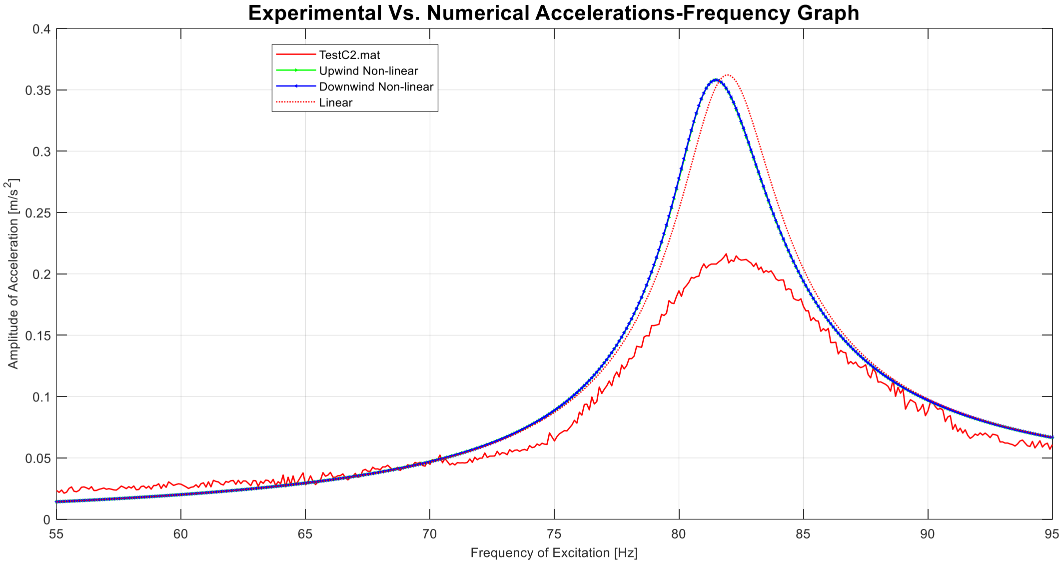
Experimental Vs. Numerical Accelerations-Frequency Graph
TestC2.mat
Upwind Non-linear
Downwind Non-linear
Linear
Amplitude of Acceleration [m/s^2]
0
0.05
0.1
0.15
0.2
0.25
0.3
0.35
0.4
55
60
65
70
75
80
85
90
95
Frequency of Excitation [Hz]

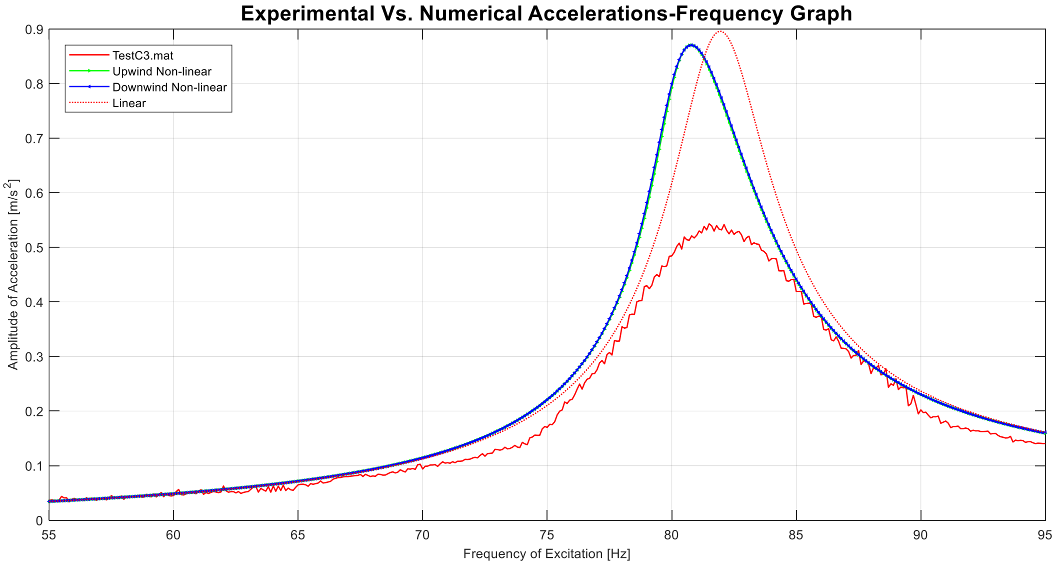
Experimental Vs. Numerical Accelerations-Frequency Graph
TestC3.mat
Upwind Non-linear
Downwind Non-linear
Linear
Amplitude of Acceleration [m/s^2]
0
0.1
0.2
0.3
0.4
0.5
0.6
0.7
0.8
0.9
55
60
65
70
75
80
85
90
95
Frequency of Excitation [Hz]

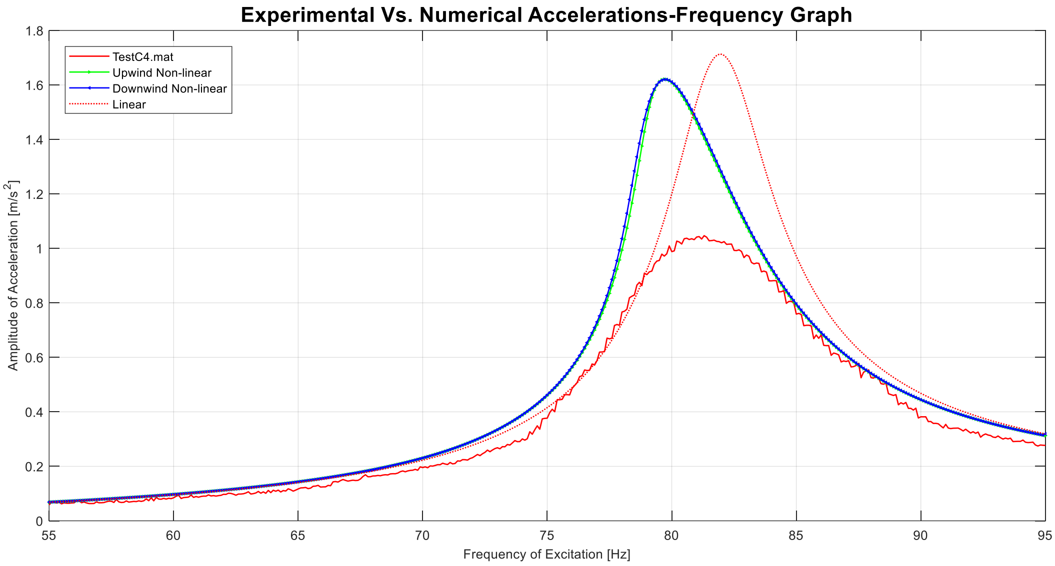
Experimental Vs. Numerical Accelerations-Frequency Graph
TestC4.mat
Upwind Non-linear
Downwind Non-linear
Linear
Amplitude of Acceleration [m/s^2]
Frequency of Excitation [Hz]
0
0.2
0.4
0.6
0.8
1
1.2
1.4
1.6
1.8
55
60
65
70
75
80
85
90
95

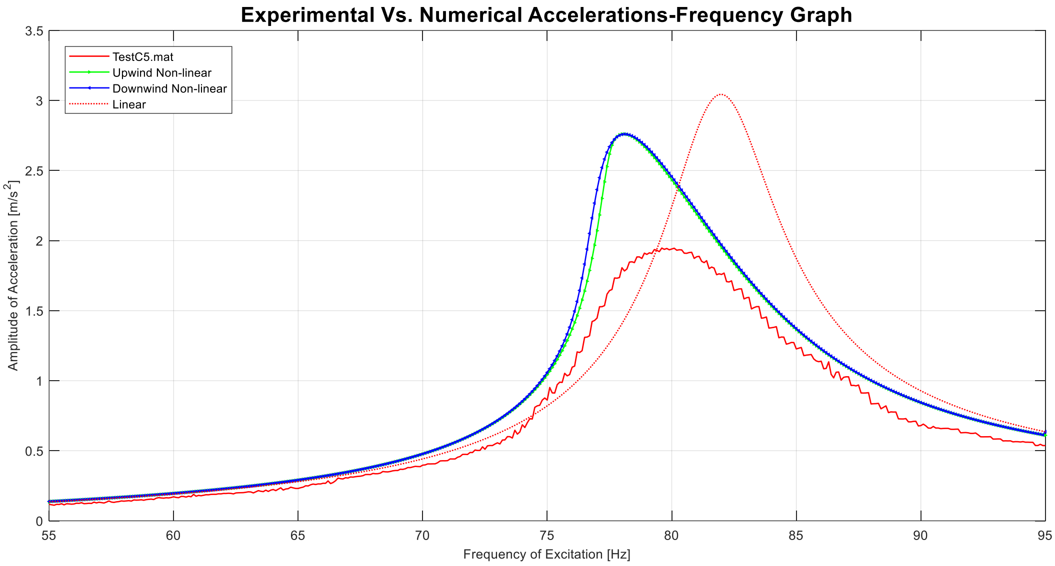
Experimental Vs. Numerical Accelerations-Frequency Graph
TestC5.mat
Upwind Non-linear
Downwind Non-linear
Linear
Amplitude of Acceleration [m/s^2]
Frequency of Excitation [Hz]
0
0.5
1
1.5
2
2.5
3
3.5
55
60
65
70
75
80
85
90
95

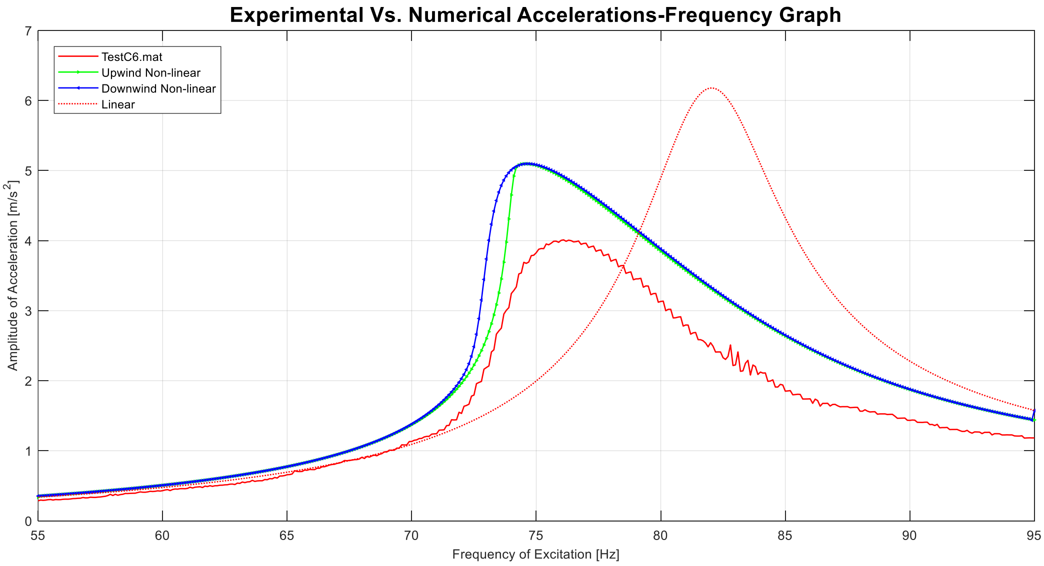
Experimental Vs. Numerical Accelerations-Frequency Graph
TestC6.mat
Upwind Non-linear
Downwind Non-linear
Linear
Amplitude of Acceleration [m/s^2]
Frequency of Excitation [Hz]
0
1
2
3
4
5
6
7
55
60
65
70
75
80
85
90
95

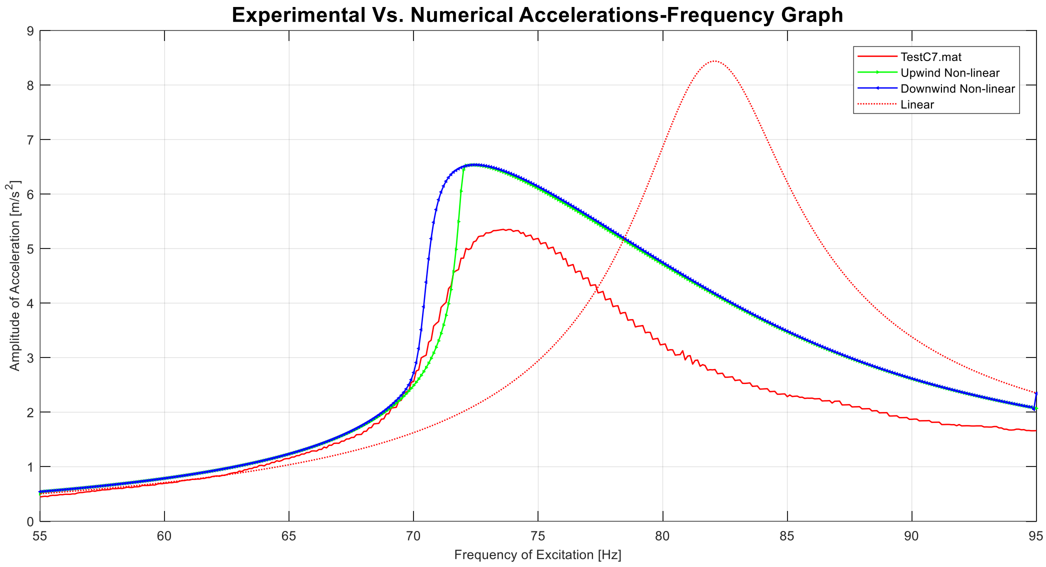
Experimental Vs. Numerical Accelerations-Frequency Graph
TestC7.mat
Upwind Non-linear
Downwind Non-linear
Linear
Amplitude of Acceleration [m/s^2]
Frequency of Excitation [Hz]
0
1
2
3
4
5
6
7
8
9
55
60
65
70
75
80
85
90
95

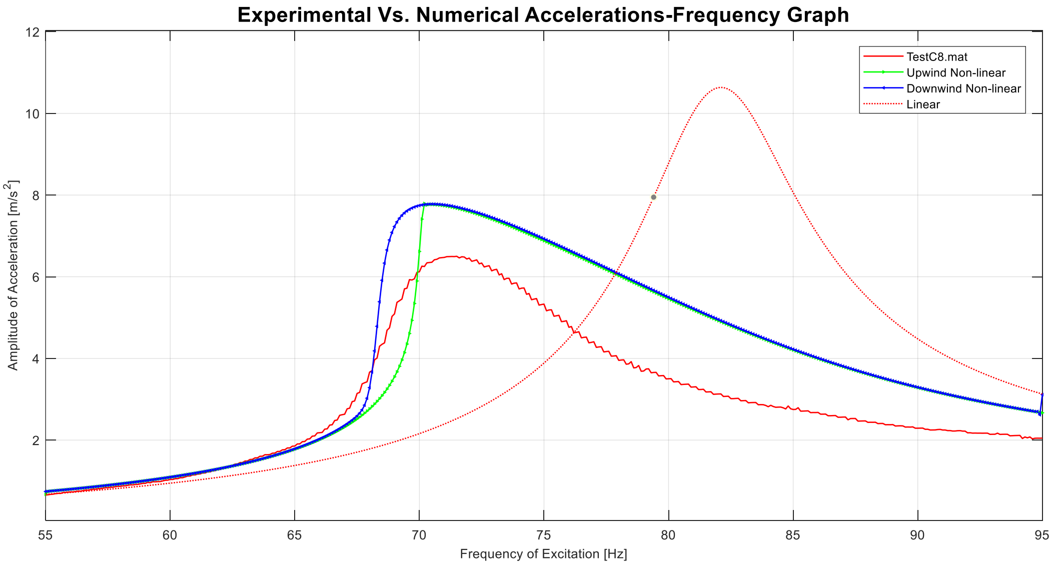
Experimental Vs. Numerical Accelerations-Frequency Graph
TestC8.mat
Upwind Non-linear
Downwind Non-linear
Linear
Amplitude of Acceleration [m/s^2]
Frequency of Excitation [Hz]
2
4
6
8
10
12
55
60
65
70
75
80
85
90
95

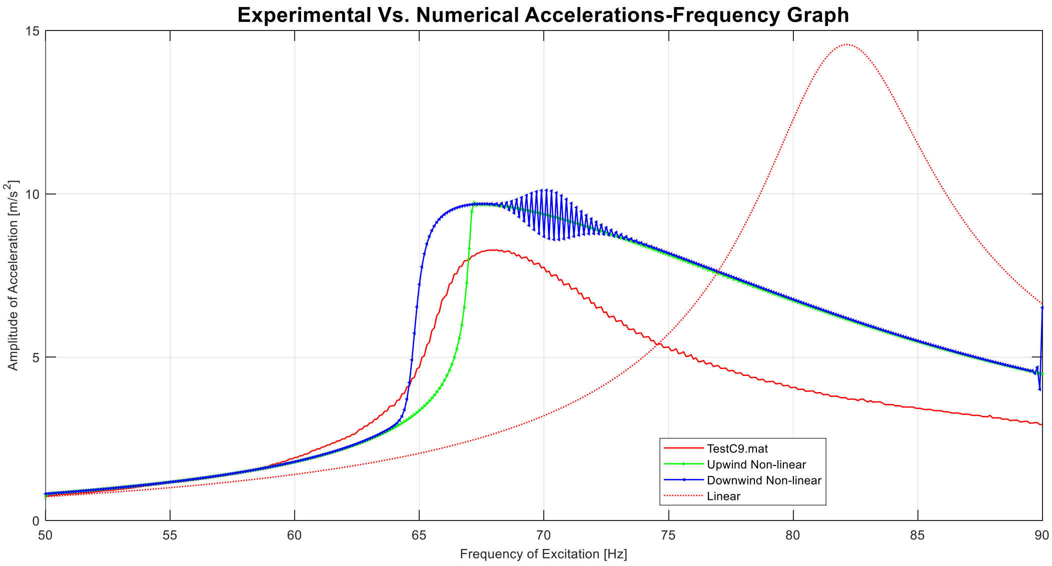
Experimental Vs. Numerical Accelerations-Frequency Graph
TestC9.mat
Upwind Non-linear
Downwind Non-linear
Linear
Amplitude of Acceleration [m/s^2]
Frequency of Excitation [Hz]
0
5
10
15
50
55
60
65
70
75
80
85
90

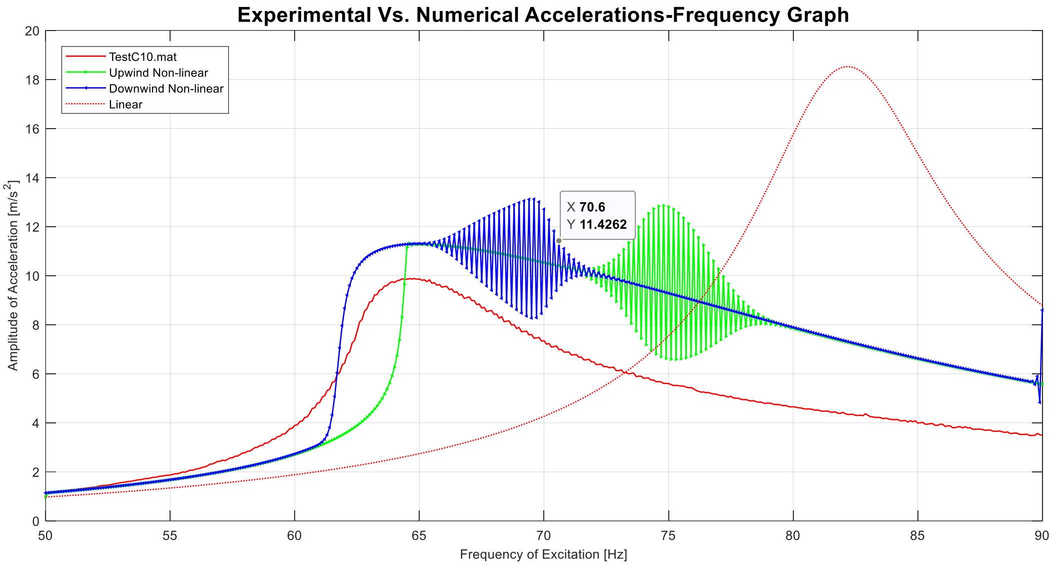
Experimental Vs. Numerical Accelerations-Frequency Graph
TestC10.mat
Upwind Non-linear
Downwind Non-linear
Linear
X 70.6
Y 11.4262
Amplitude of Acceleration [m/s^2]
Frequency of Excitation [Hz]
0
2
4
6
8
10
12
14
16
18
20
50
55
60
65
70
75
80
85
90

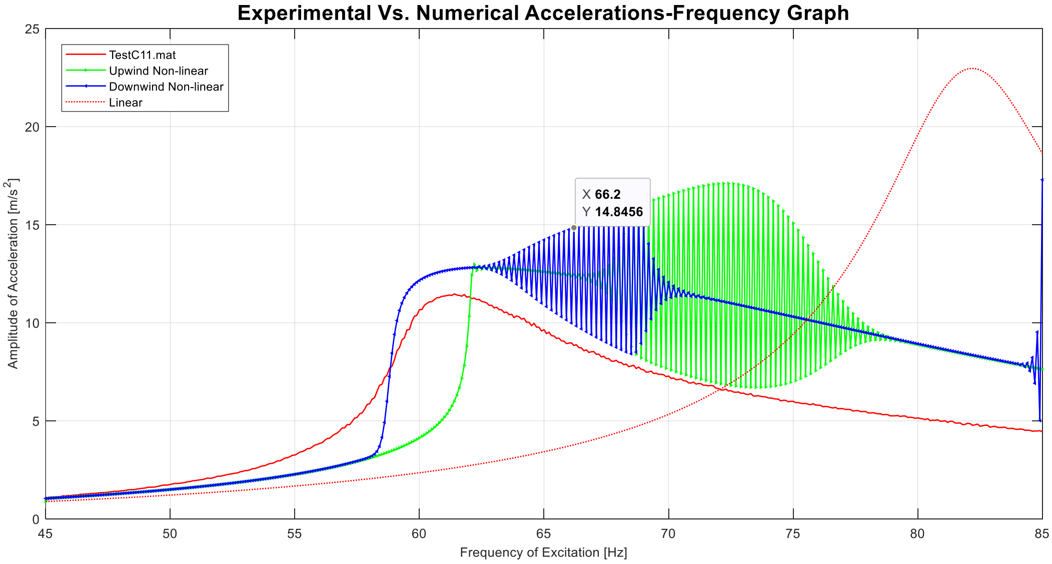
Experimental Vs. Numerical Accelerations-Frequency Graph
TestC11.mat
Upwind Non-linear
Downwind Non-linear
Linear
X 66.2
Y 14.8456
Amplitude of Acceleration [m/s^2]
Frequency of Excitation [Hz]
0
5
10
15
20
25
45
50
55
60
65
70
75
80
85

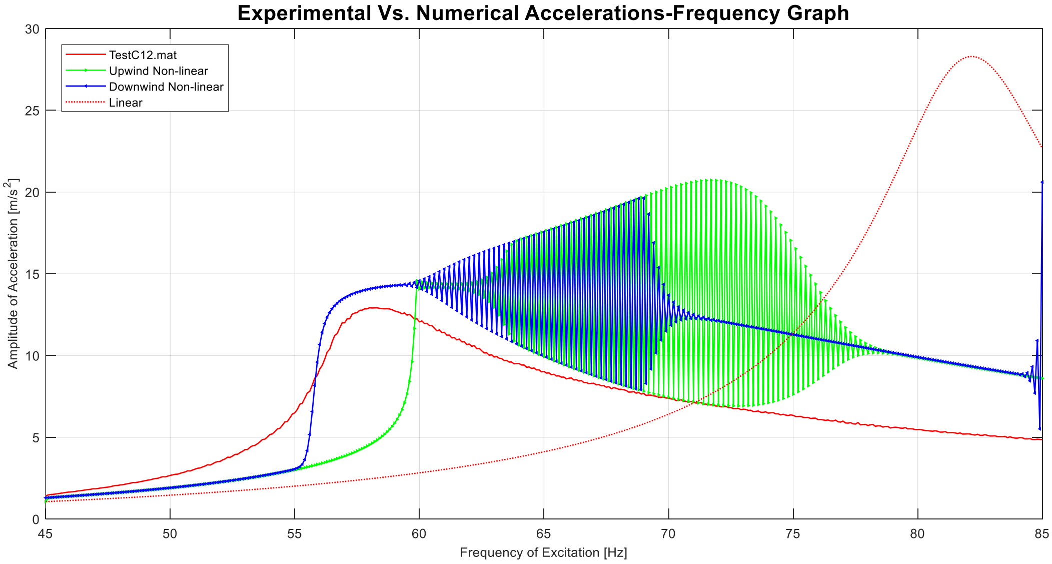
Experimental Vs. Numerical Accelerations-Frequency Graph
TestC12.mat
Upwind Non-linear
Downwind Non-linear
Linear
Amplitude of Acceleration [m/s^2]
Frequency of Excitation [Hz]
0
5
10
15
20
25
30
45
50
55
60
65
70
75
80
85

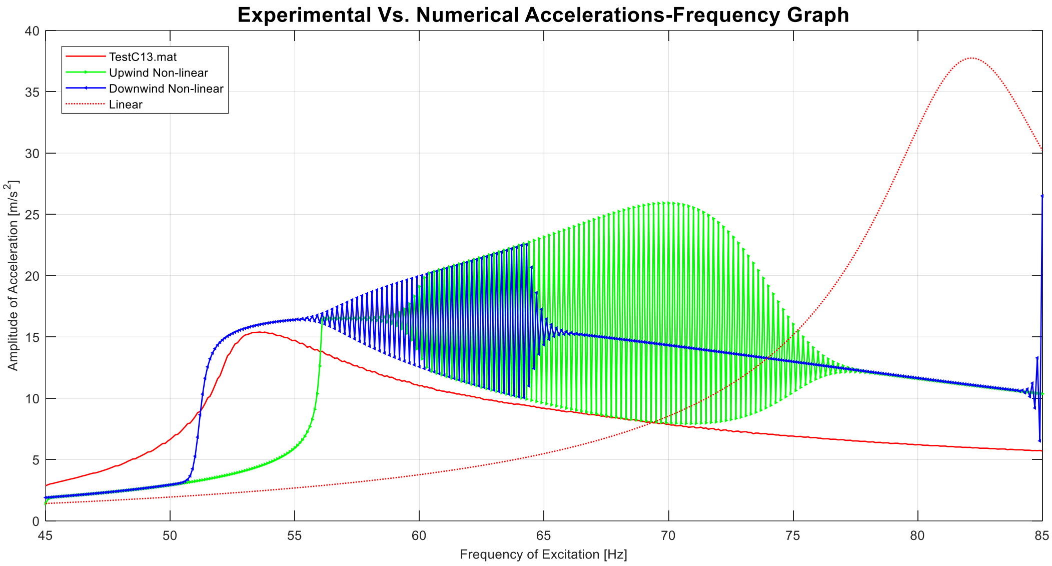
Experimental Vs. Numerical Accelerations-Frequency Graph
TestC13.mat
Upwind Non-linear
Downwind Non-linear
Linear
Amplitude of Acceleration [m/s²]
0
5
10
15
20
25
30
35
40
Frequency of Excitation [Hz]
45
50
55
60
65
70
75
80
85

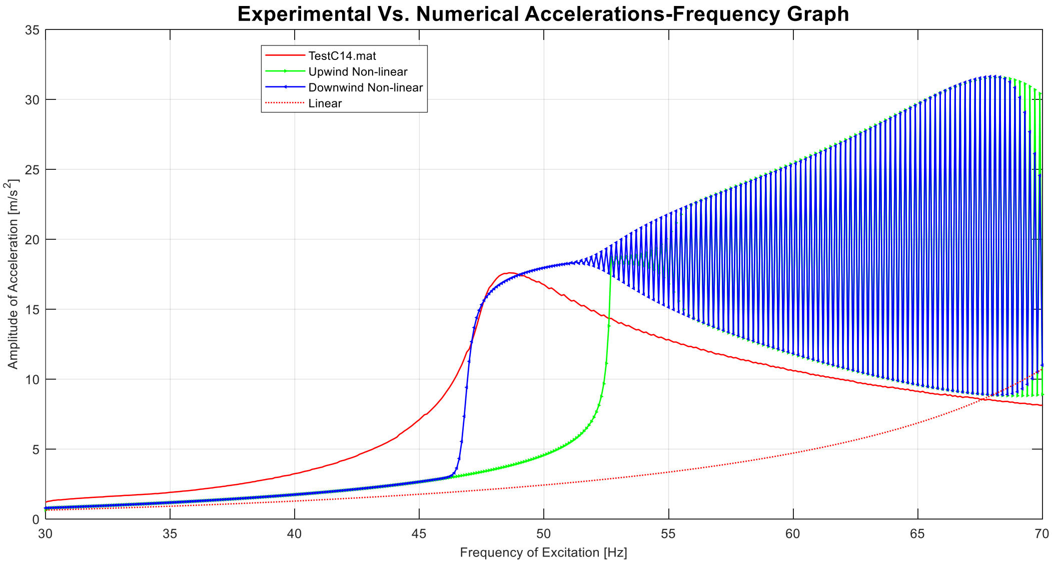
Experimental Vs. Numerical Accelerations-Frequency Graph
TestC14.mat
Upwind Non-linear
Downwind Non-linear
Linear
Amplitude of Acceleration [m/s²]
0
5
10
15
20
25
30
35
Frequency of Excitation [Hz]
30
35
40
45
50
55
60
65
70

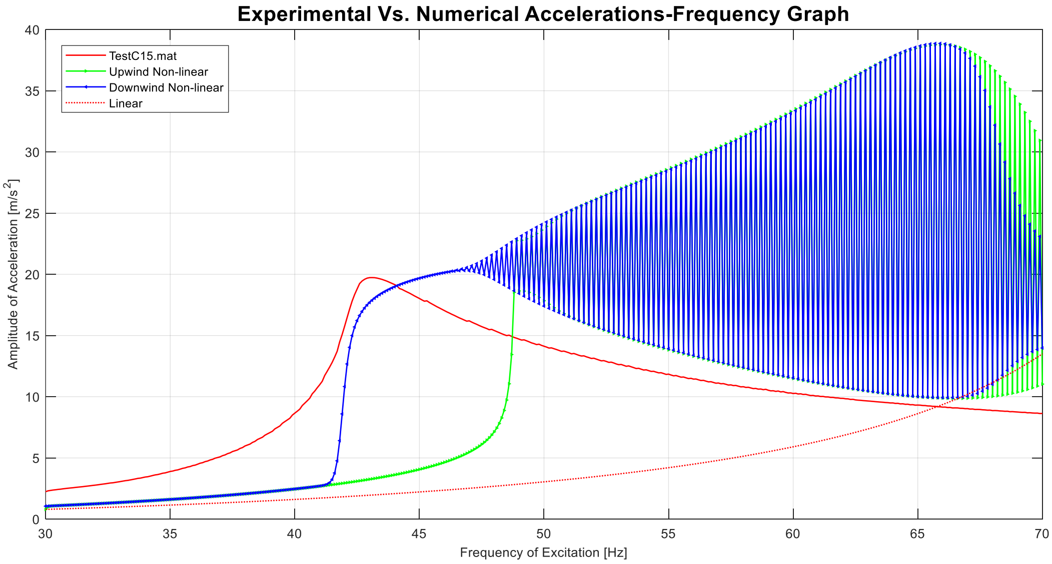
Experimental Vs. Numerical Accelerations-Frequency Graph
TestC15.mat
Upwind Non-linear
Downwind Non-linear
Linear
Amplitude of Acceleration [m/s²]
0
5
10
15
20
25
30
35
40
Frequency of Excitation [Hz]
30
35
40
45
50
55
60
65
70

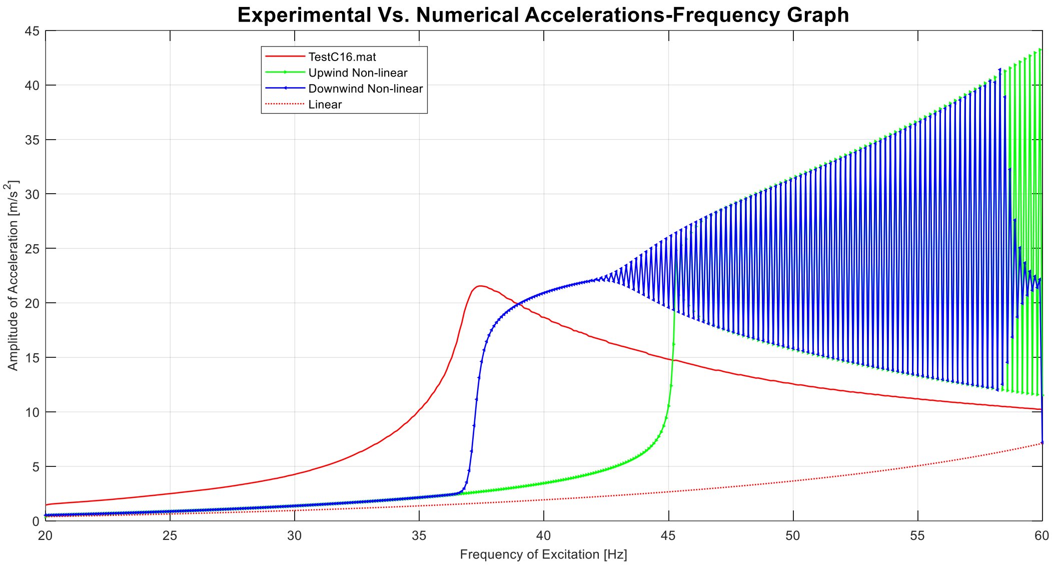
Experimental Vs. Numerical Accelerations-Frequency Graph
TestC16.mat
Upwind Non-linear
Downwind Non-linear
Linear
Amplitude of Acceleration [m/s^2]
Frequency of Excitation [Hz]
0
5
10
15
20
25
30
35
40
45
20
25
30
35
40
45
50
55
60

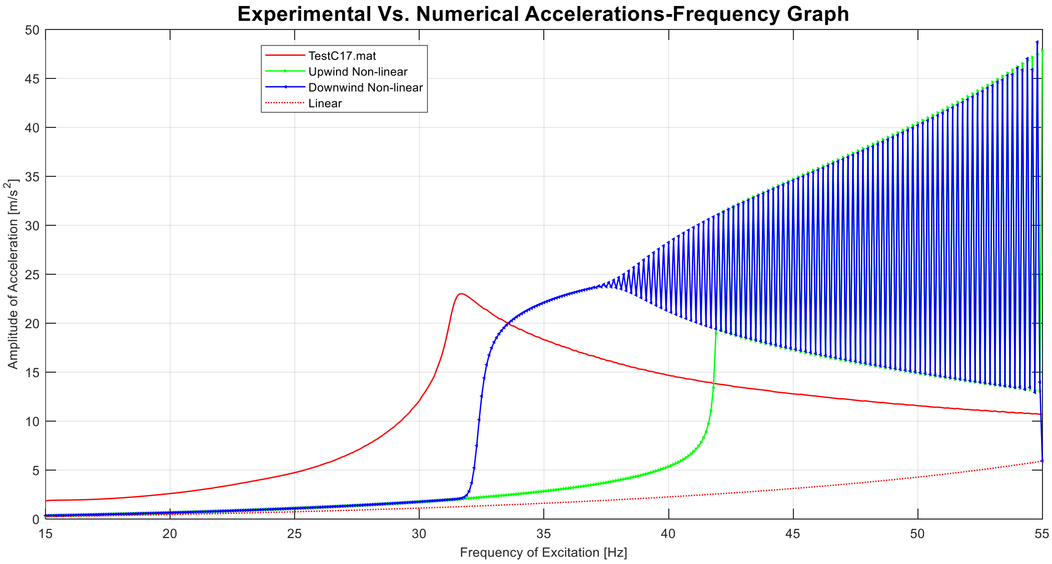
Experimental Vs. Numerical Accelerations-Frequency Graph
TestC17.mat
Upwind Non-linear
Downwind Non-linear
Linear
Amplitude of Acceleration [m/s^2]
Frequency of Excitation [Hz]
0
5
10
15
20
25
30
35
40
45
50
15
20
25
30
35
40
45
50
55